





Lepto-Hadronic Scenarios for TeV Extensions of Gamma-Ray Burst Afterglow Spectra

MARC KLINGER ¹, CHENGCHAO YUAN (袁成超) ¹, ANDREW M. TAYLOR ¹ AND WALTER WINTER ¹

¹*Deutsches Elektronen-Synchrotron DESY, Platanenallee 6, 15738 Zeuthen, Germany*

ABSTRACT

Recent multi-wavelength observations of gamma-ray burst afterglows observed in the TeV energy range challenge the simplest Synchrotron Self-Compton (SSC) interpretation of this emission, and are consistent with a single power-law component spanning over eight orders of magnitude in energy. To interpret this generic behaviour in the single-zone approximation without adding further free parameters, we perform an exhaustive parameter space study using the public, time-dependent, multi-messenger transport software AM³. This description accounts for the radiation from non-thermal protons and the lepto-hadronic cascade induced by pp - and $p\gamma$ -interactions. We summarise the main scenarios which we have found (*SSC*, *Extended-syn*, *Proton-syn*, *pp-cascade*, and *p γ -cascade*), and discuss their advantages and limitations. We find that possible high-density environments, as may be typical for surrounding molecular cloud material, offer an alternative explanation for producing flat hard (source) spectra up to and beyond energies of 10 TeV.

Keywords: Classical Novae (251) — Ultraviolet astronomy(1736) — History of astronomy(1868) — Interdisciplinary astronomy(804)

1. INTRODUCTION

Recent detections of gamma-ray bursts (GRBs) with photons in the very-high-energy (VHE; 0.1-100 TeV) regime have opened a new opportunity to test the capability of particle acceleration at relativistic shocks (H.E.S.S. Collaboration et al. 2019; MAGIC Collaboration et al. 2019a; H. E. S. S. Collaboration et al. 2021; LHAASO Collaboration et al. 2023).

The typical observational signature of a GRB consists of an early (few to few hundred seconds), bright prompt emission phase during which complex temporal behaviour is observed. This is followed by an afterglow emission phase, during which the light curve decays in a smooth (sometimes broken) power-law shape, which can be observed for much longer (up to months) depending on the sensitivity of the observing instrument. While the origin of the prompt emission is still under debate – see, e.g., Mochkovitch & Daigne (1998); Kobayashi et al. (1997); Giannios & Spruit (2005); Zhang & Yan (2011); Beloborodov & Mészáros (2017); Pe’er & Ryde (2018); Ghisellini et al. (2020) – the afterglow emission is commonly believed to emerge from a relativistic shock set up at the interface between a fast outflow, typically called blast wave, and its surrounding medium (for reviews see, e.g., Piran 2004; Mészáros 2006; Zhang 2018). The simultaneous generation of turbulent magnetic fields, and

the acceleration of charged electrons that cool via synchrotron radiation, results in a plausible explanation for the observations of afterglows from sub eV up to multi GeV energies.

A widely established, but constraining assumption in the modelling, is to assume that the dissipation of bulk kinetic energy into radiation can be described in a single, homogeneous, and isotropic region (the one-zone approximation; see, e.g., Zhang 2018). This has the advantage of only a handful ($\sim 5 - 10$) of free parameters and allows for a broken power-law description of the spectral energy distributions (SEDs) observed from often sparse eV to GeV data (below these energies typically a less certain reverse shock component is included). However, this synchrotron component is commonly expected to not reach far above GeV energies (so called synchrotron burn-off), limited by the interplay of acceleration and radiation by the same magnetic field.

The new clear detection of VHE emission of multiple long GRBs offers a novel level of spectral information up to unprecedentedly high photon energies. This allows one to critically address the question as to the production mechanism of the emission in the VHE band, in particular if a new spectral component is required.

A common interpretation of the VHE emission is that these are synchrotron photons which are inverse-Compton up-scattered to the VHE band by the same

population of electrons (the one-zone synchrotron self-Compton (SSC) scenario, e.g., Meszaros et al. 1994; Chiang & Dermer 1999; Sari & Esin 2001). The observational picture, namely hard (spectral) photon indices extending up to energies of 10 TeV (see Section 2), raise problems with this interpretation due to the spectral softening by the Klein-Nishina effects in the cross-section (see Section 4.1).

Besides the simple SSC interpretation, a variety of other mechanisms has been proposed, which are departing from the single zone approximation to multi-zone models. This includes for example multiple/decaying magnetic fields (e.g. Khangulyan et al. 2021, 2023; Grošelj et al. 2022; Vanthieghem et al. 2020), external Compton scenarios (Murase et al. 2018; Zhang et al. 2020, 2021; Yuan et al. 2022), a reverse shock component (e.g. Zhang et al. 2023a), structured jets (e.g. Gill & Granot 2023; Sato et al. 2023; O'Connor et al. 2023), a significant role of the precursor (Vanthieghem et al. 2020) and far upstream regions (Beloborodov 2002; Derishev & Piran 2016), as well as cascades along the propagation to Earth (e.g. Das & Razzaque 2023). We highlight that many of these ideas require new parameters, that could be hard to justify by the current quality of the observational data. Instead, it is necessary to first systematically explore the possibilities of the one-zone model to reproduce the emerging single power-law observations.

Besides the non-thermal electrons, there are multiple reasons to expect ions to be accelerated at the relativistic shock as well. GRBs are a common candidate of ultra-high-energy (UHE; $\gtrsim 10^{18}$ eV) cosmic-ray accelerators (Waxman 1995; Vietri 1995; Bell et al. 2018), their surrounding interstellar or stellar-wind medium is expected to be ion dominated, and ion acceleration is also seen in short-time-scale microphysics simulations (e.g. Marcowith et al. 2016). This leads to a range of additional channels to dissipate the kinetic energy to radiation. We therefore explore the potential of lepto-hadronic signatures in the one-zone approximation to explain the VHE emission, and limit ourselves for simplicity to the injection of protons (and electrons).

One possible channel, the synchrotron radiation of non-thermal protons, has been discussed in the literature without a coherent conclusion (H.E.S.S. Collaboration et al. 2019; MAGIC Collaboration et al. 2019b; H. E. S. S. Collaboration et al. 2021; Isravel et al. 2023b,a; Cao et al. 2023).

As a different channel, electromagnetic cascades inside the source initiated at energies above the VHE regime via photo-hadronic or proton-proton interactions, are other ideas to generate SEDs up to energies > 10 TeV

Observed fluxes and comoving densities

$EF_E \propto E^2 \frac{dN}{dE}$	Observed photon energy flux
$\hat{n}'_E \propto \frac{dN'}{dE'}$	Particle spectral density

Power-law indices

γ with $EF_E \propto E^{2-\gamma}$	Photon index
s with $\hat{n}'_E \propto E'^{-s}$	Spectral index (electrons, protons)
s_{inj} with $q'_E \propto E'^{-s_{\text{inj}}}$	Injection spectral index

Primed	Frame momentarily comoving with blast wave
Un-primed	Observed frame
Star \star	Progenitor rest frame

Table 1. Notation used in this paper

(for a $p\gamma$ model see, e.g., Wang et al. 2023). From the observational perspective, see Section 2, this is particularly interesting, as cascades naturally yield power-law spectra with photon indices of $\gamma \approx 2$ (similar to Berezhinsky & Kalashev 2016). Note, that in this paper we use the notation $EF_E \propto E^{2-\gamma}$, see Table 1.

We note that these lepto-hadronic ideas would also lead to neutrino signatures from the afterglow, although this has been recently found to be observationally not very promising for some cases (Guarini et al. 2023).

These conceptual ideas necessitate a systematic exploration of the potential of lepto-hadronic one-zone models to explain the emerging observational picture of hard ($\gamma \approx 2$) photon SEDs, that also resemble a single power-law component spanning from keV to TeV energies. We give a summary of the observational picture in Section 2. We then discuss our model for the emission in Section 3 and present the representative scenarios we found in Section 4. Finally, we discuss their implications in Section 5, and conclude in Section 6.

2. OBSERVATIONAL PICTURE AT THE HIGHEST ENERGIES

We focus in this work on the window from keV to TeV energies, where the observations are not severely absorbed, see Section 3.3 for details.

Up to which energies the afterglow radiation can be observed has been a topic of speculation for a long while. A first observational hint was given by the detection of the unprecedentedly bright GRB 130427A up to ~ 100 GeV energies with a photon index of $\gamma \sim 2$ ($EF_E \propto E^{2-\gamma}$), however resulting in no clear detection at VHE (Ackermann et al. 2014; Kouveliotou et al. 2013).

More recently the afterglows of multiple GRBs in the VHE band have been detected with high significance.

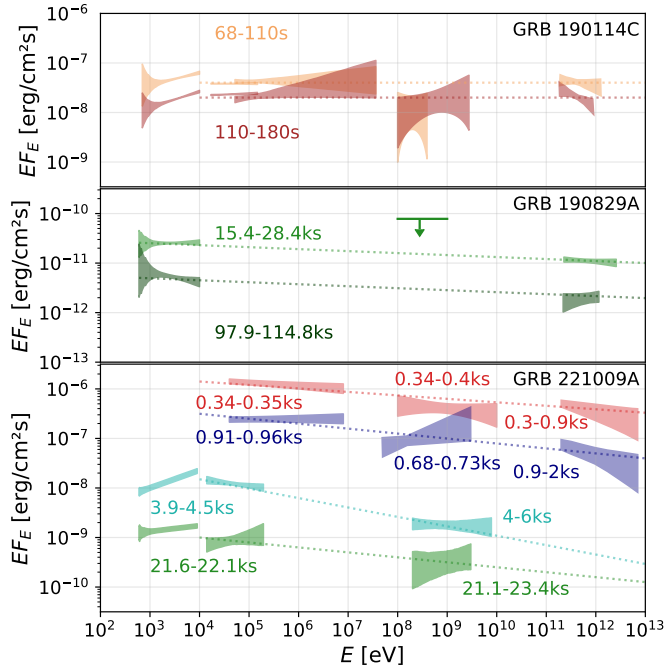


Figure 1. Observational picture of the three GRB afterglows detected at VHE with highest level of spectral information: GRB 190114C, GRB 190829A, and GRB 221009A. Dotted lines indicate the emerging power-law behaviour discussed in the text. The data is compiled from Klinger et al. (2023a); Ajello et al. (2020); MAGIC Collaboration et al. (2019b); H. E. S. S. Collaboration et al. (2021); LHAASO Collaboration et al. (2023); Zhang et al. (2023b); Liu et al. (2023); Tavani et al. (2023); Klinger et al. (2024). All times refer to the corresponding *Fermi*-GBM trigger time.

We focus here on the three GRBs with the best measurements of the VHE photon index and broad multi-wavelength (MWL) coverage. We summarise their contemporaneous keV–TeV SEDs in Figure 1 and discuss the observational picture for each of them in the following.

GRB 190114C—In the VHE regime, this GRB was detected particularly early, around 1 min after initial trigger, by the Major Atmospheric Gamma Imaging Cherenkov (MAGIC) telescopes (MAGIC Collaboration et al. 2019a). However, the challenging observational conditions with bright moonlight and the extragalactic-background-light (EBL) absorption due to the intermediate distance (redshift $z = 0.43$) limited an estimation of the de-absorbed photon index at TeV energies to $\gamma = 1.9 \pm 0.4(\text{stat})_{-0.1}^{+0.2}(\text{sys})$ for 62–100 s after the trigger, and $\gamma = 2.2_{-0.4}^{+0.5}(\text{stat}) \pm 0.3(\text{sys})$ for 100–140 s after trigger (see Extended Data Table 1 of MAGIC Collaboration et al. 2019a). Besides the VHE data, the contemporaneous MWL coverage for this GRB spans a broad

range from keV to GeV energies, including data from the *Swift* X-ray Telescope (*Swift*-XRT), *Swift* Burst Alert Telescope (*Swift*-BAT), *Fermi* Gamma-Ray Burst Monitor (*Fermi*-GBM), and the *Fermi* Large Area Telescope (*Fermi*-LAT), see Ajello et al. (2020); MAGIC Collaboration et al. (2019b); Klinger et al. (2023a). It should be noted, that the photon statistics in *Fermi*-LAT are only 5 and 6 photons in the envelopes shown in Figure 1. *Fermi*-LAT, therefore, does not significantly constrain the combined MWL SED (Klinger et al. 2023a). Remarkably, this SED appears to be consistent with a single power-law component with photon index $\gamma \approx 2$ decaying consistently in time from keV to TeV energies (indicated by the dotted lines in Figure 1, see also Ajello et al. (2020)). Even though widely attributed to a two component synchrotron self-Compton (SSC) origin (e.g. MAGIC Collaboration et al. 2019b; Asano et al. 2020; Derishev & Piran 2021), a more sophisticated statistical test on the counts-level shows no robust preference over a single component origin, in particular when including the cross-calibration uncertainties from the multiple instruments (Klinger et al. 2023a). This leads us to conclude that the large MWL data set is indicative of a single power-law photon spectrum, but remains inconclusive of the origin of the VHE emission.

GRB 190829A—The afterglow of this GRB was detected relatively late in the VHE band with the High Energy Stereoscopic System (H.E.S.S.), at about 4–8 hours (first night corresponding to 15.4–28.4 ks) and 27–32 hours (second night corresponding to 97.9–11.8 ks) (H. E. S. S. Collaboration et al. 2021). However, the proximity of the event ($z = 0.08$) allowed for a relatively precise measurement of the de-absorbed photon index at VHE, yielding $\gamma = 2.1 \pm 0.1(\text{stat}) \pm 0.3(\text{sys})$ (night 1) and $\gamma = 1.9 \pm 0.3(\text{stat}) \pm 0.2(\text{sys})$ (night 2). Unfortunately, at such late times the contemporaneous MWL coverage is limited to only *Swift*-XRT at keV energies. Remarkably, extrapolation of both individual spectra by a power-law of photon index $\gamma \approx 2.1$ are consistent with each other (indicated by the dotted lines in Figure 1), leading to a similar picture as for GRB 190114C above. A statistical test on the counts-level basis prefers a single synchrotron component at $> 5\sigma$ (H. E. S. S. Collaboration et al. 2021). Assuming a single radiation zone, this tension is mainly driven by the hard spectrum observed in the VHE band being in contrast with the expectation of a softer SSC component, softened by the Klein-Nishina effects. This leads us to conclude that this MWL data set is consistent with a single power-law photon spectrum, and in tension with a one-zone SSC scenario as the origin of the VHE emission.

GRB 221009A—This event is the brightest GRB detected so far, and was followed up by a large amount of MWL observations. It triggered *Fermi*-GBM (we use this as T_0) about 225 s before the main burst saturated the detector. The event was detected by the Large High Altitude Air Shower Observatory (LHAASO), where the combined data sets of the Water Cherenkov Detector Array (WCDA) and the Kilometer Squared Array (KM2A) show a single power-law with de-absorbed photon index ($\gamma \approx 2.35 \pm 0.03(\text{stat})$ for 230-300 s after trigger, and $\gamma \approx 2.26 \pm 0.02(\text{stat})$ for 300-900 s after trigger), which extends from 0.2 TeV up to at least 10 TeV (LHAASO Collaboration et al. 2023; Cao et al. 2023). With a redshift of $z = 0.15$, the EBL absorption introduces systematic uncertainties to the de-absorbed photon index of at least 0.1, and limits robust conclusions towards the intrinsic spectral shape at energies above 10 TeV. Due to the smoothly varying lightcurve detected with the WCDA, the emission is commonly attributed to the early afterglow phase. This hard VHE spectrum itself is again challenging to describe within an SSC scenario, again due to the Klein-Nishina spectral softening effects expected. In addition, a time and energy dependent analysis of the contemporaneous *Fermi*-GBM data indicates a hard afterglow component showing up in light-curve valleys between the prompt signatures (Lesage et al. 2023; Zhang et al. 2023b). Remarkably, the spectra of *Fermi*-GBM and LHAASO are compatible with a single power-law component with a photon index of $\gamma \approx 2.1 - 2.2$ (see again indicative dotted lines in Figure 1). Taking into account the observational challenges introduced by the viewing angle through the Galactic plane (e.g. Klinger et al. 2024), this conclusion is also consistent with the observations by *Fermi*-LAT and the instruments on board of the AGILE satellite (Liu et al. 2023; Tavani et al. 2023), although a prompt origin of this emission cannot be excluded. A comparison of this picture to later observations (4 ks, 22 ks) of *Swift*-XRT, *Swift*-BAT, and *Fermi*-LAT also shows consistency with a power-law of photon index $\gamma \approx 2.2$ (see Klinger et al. 2024, for a counts-level MWL fit). This leads us to conclude that this large MWL data set is indicative of a single power-law photon spectrum, and is in tension with a one-zone SSC scenario as the origin of the VHE emission.

In summary, we find an emerging observational picture of photon spectra resembling a single power-law component extending from roughly keV to sometimes even tens of TeV energies, and with a hard photon index of $\gamma \approx 2 - 2.2$.

Population Picture—Putting these observations into the context of the population of GRBs with detection up to only GeV energies (though without constraining VHE upper limits), one finds that the picture inferred from the VHE detected GRB is not particularly unique. Looking at the 2nd GRB catalogue from *Fermi*-LAT (Ajello et al. 2019), one finds for their afterglow emission (“EXT”) window an average photon index of $\gamma \approx 2$ too, although with a large spread (10%/90% percentile of 1.6/2.5). Taking all *Swift*-XRT-detected GRBs, and the subset also detected by *Fermi*-LAT, the photon index distribution at keV energies peaks around $\gamma \approx 2$ and $\gamma \approx 1.8$, respectively (Ajello et al. 2018). This indicates that a spectral break typically occurs somewhere in this keV-MeV energy range or below, and that the hard power-law spectrum commonly observed at the highest energies extends also down to X-ray energies on average.

3. METHODS

In this section we describe how we model the observed afterglow emission. We do this by performing the blast wave modelling independently from the radiation modelling and ignore the feedback from the radiation on the blast wave. This has been done in many works; see, e.g., Zhang (2018) for a review.

We discuss in Section 3.1 our description of the circumstances in the blast wave. These provide the conditions for our multi-messenger radiation modelling in this radiation zone (Section 3.2), where we use the open-source software AM³ for the first time also to perform GRB afterglow modelling. Then, we discuss in Section 3.3 how we convert our radiation densities to observed spectra and the expected propagation effects during their way to Earth. Finally, we summarise our performed parameter space exploration and qualitative scenario type selection in Section 3.4.

For better reproducibility of our results, we publish the source code for our scenarios on GitHub¹.

3.1. Shock Description, Blast Wave Dynamics, One-Zone approximation

In our definition, the blast wave refers to a thin shell immediately downstream of the relativistic shock. We approximate this shock as an infinitely thin discontinuity, and ignore the effects of magnetic fields, non-thermal particles, and radiation pressure on the jump conditions. Motivated by micro-physical simulations, we also assume that the shock discontinuity amplifies turbulent magnetic fields and accelerates particles, producing a non-thermal (power-law) spectrum between a

¹ <https://github.com/maklinger/LepHadGRBAfterglows>

minimum and maximum energy. We highlight that this set of assumptions — commonly used in the GRB literature — is only accurate to factors of order unity, $\mathcal{O}(1)$, see also Section 5.1. Consequently, we keep the focus on the dominant scaling relations and ignore details of order unity factors for the rest of the paper.

The instantaneous conditions in the blast wave, relevant for the radiation modelling, are defined via the Lorentz factor of the shock Γ , observation time t , and proton number density just upstream the shock n . We define the (momentarily comoving) dynamical timescale $t'_{\text{dyn}} = \Gamma t$ (Doppler factor $\mathcal{D} \approx \Gamma$, we ignore the redshift factor $(1+z) \approx \mathcal{O}(1)$) and the upstream ram pressure $p'_{\text{ram}} = \Gamma^2 n m_p c^2$ with the average upstream particle mass taken to be the proton mass m_p . With this we can define the timescale for the free-streaming escape of uncharged particles t'_{esc} , the adiabatic cooling t'_{adi} of charged particles (coupled via the magnetic fields), and the timescale of volume dilution t'_{exp} introduced by the expansion of the blast wave:

$$t'_{\text{esc}} \approx t'_{\text{adi}} \approx t'_{\text{exp}} \approx t'_{\text{dyn}} \approx \Gamma t \quad (1)$$

$$= 3 \times 10^4 \text{s} \left(\frac{\Gamma}{30} \right) \left(\frac{t}{10^3 \text{s}} \right) \quad (2)$$

As a pp target, we estimate the thermal proton density in the blast wave as n' from the shock jump conditions, and ignore their momentum compared to non-thermal protons (cold target approximation).

$$n' \approx \Gamma n = 30 \text{cm}^{-3} \left(\frac{\Gamma}{30} \right) \left(\frac{n}{1 \text{cm}^{-3}} \right) \quad (3)$$

We parameterise the isotropic magnetic field pressure p'_B and the non-thermal proton/electron injection in terms of the ram pressure p'_{ram} via the fractions² $\varepsilon_{B/p/e} \ll 1$:

$$p_{B/e/p} = \varepsilon_{B/e/p} \Gamma^2 n m_p c^2 \quad (4)$$

This defines our magnetic field strength B' :

$$B' = 0.6 \text{G} \left(\frac{n}{1 \text{cm}^{-3}} \right)^{1/2} \left(\frac{\Gamma}{30} \right) \left(\frac{\varepsilon_B}{10^{-2}} \right)^{1/2} \quad (5)$$

We furthermore assume the non-thermal particle injection spectra $q'_{e/p}$ to be of a power-law form with spectral index s_{inj} for electrons and protons, an exponential cut-off at $E'_p{}^{\text{max}}$ (protons) and $E'_e{}^{\text{max}}$ (electrons), and a step-like cut-on above the minimum energy

$E'_e{}^{\text{min}} = E'_p{}^{\text{min}} \equiv E'_{\text{min}}$ (same free parameter for both³). Thus:

$$\begin{aligned} q'_{E,e/p} &\equiv \frac{d^3 N'_{e/p}}{dt' dV' dE'_{e/p}} \\ &= q'_{E,\text{min}} \left(\frac{E'_{e/p}}{E'_{\text{min}}} \right)^{-s_{\text{inj}}} \exp \left(-\frac{E'_{e/p}}{E'_{e/p}{}^{\text{max}}} \right) \quad (6) \\ &\quad \text{for } E'_{e/p} \geq E'_{\text{min}}, \end{aligned}$$

with $q'_{E,\text{min}}$ defined via

$$\int dE'_{e/p} E'_{e/p} q'_{E,e/p} = \frac{\varepsilon_{e/p} p'_{\text{ram}}}{t'_{\text{dyn}}}. \quad (7)$$

We re-parameterise the maximum energy in terms of the Bohm parameter η (Bohm 1949), by balancing the acceleration time $t'_{\text{acc}} = \eta E'_{e/p} / (e B' c)$ (with electron/proton charge e , speed of light c , and t'_{acc} dominated by the downstream component of the acceleration cycle) to the fastest cooling time at a given instance (computed via AM³, see Section 3.2).

In order to perform time-dependent radiation modelling, i.e. including the evolution of the blast wave parameters with time, the blast wave dynamics (i.e. Γ as a function of t) are needed. This requires further assumptions on the density profile through which the blast wave passes. For simplicity, we consider a constant density case in the power-law deceleration regime (Blandford & McKee 1976):

$$\begin{aligned} \Gamma &\approx \left(\frac{3}{2^8 \pi m_p c^5} \frac{E_{\text{kin,iso}}}{n t^3} \right)^{1/8} \\ &\approx 56 \left(\frac{n}{1 \text{cm}^{-3}} \right)^{-1/8} \left(\frac{E_{\text{kin,iso}}}{10^{54} \text{erg}} \right)^{1/8} \left(\frac{t}{10^3 \text{s}} \right)^{-3/8} \end{aligned} \quad (8)$$

Our normalisation is obtained by the conservation of the initial kinetic energy $E_{\text{kin,iso}}$:

$$E_{\text{kin,iso}} \approx \Gamma(t)^2 m_{\text{sw}}(r_*(t)) c^2 \quad (9)$$

with the isotropic-equivalent swept-up mass $m_{\text{sw}}/4\pi = m_p \int dr_* r_*^2 n(r_*)$, $r_*(t) = 4\Gamma(t)^2 t c$ and $\mathcal{D} \approx \Gamma$.

3.2. Multimessenger Modelling

The evolution of the spectral and spatial density $\hat{n}'_{E,i} = d^2 N'_i / dE'_i dV'$ of each considered particle species

² For the hydrodynamic shock approximation these pressures need to be negligible to the dynamics of the system (e.g. compared to the proton thermal pressure)

³ We note that, motivated by the large uncertainty, we use the injection energy scale, E'_{min} , as a free parameter, rather than the often adopted constant fraction parameters (e.g. Sari et al. 1996): the non-thermal particle number (ζ) and energy injection (ε) rates (e.g. van der Horst et al. 2014; Misra et al. 2021; Warren et al. 2015, 2018; Ressler & Laskar 2017; Asano et al. 2020).

i involves the temporal evolution of a system of coupled transport equations of the following form:

$$\frac{\partial \hat{n}'_E}{\partial t} = -\frac{\partial}{\partial E'} \left(\frac{E \hat{n}'_E}{\tau'_{\text{cool}}} \right) - \frac{\hat{n}'_E}{\tau'_{\text{sink}}} + q'_E \quad (10)$$

This requires the estimation of the time scales of the relevant cooling processes τ'_{cool} , and sink/loss/escape processes τ'_{sink} , as well as the injection terms q'_E . All three can be in principle a function of time and energy, and can depend on the density of other species. We use AM³ to calculate these terms, and to evolve in time the densities of protons, neutrons, electrons, positrons, pions, muons, neutrinos and photons as a combined system. As explained in detail in Gao et al. (2019) and Klinger et al. (2023b), we include synchrotron and inverse Compton cooling and emission of all charged particles, synchrotron self-absorption of electrons and positrons, photon-photon annihilation ($\gamma\gamma \rightarrow e^+e^-$) including pair feedback, escape of neutral particles and adiabatic cooling of charged particles, photohadronic ($p\gamma \rightarrow \pi\dots$) and proton-proton ($pp \rightarrow \pi\dots$) induced pion production, the subsequent decays of pions and muons and the electron-positron pair production via the Bethe-Heitler process ($p\gamma \rightarrow pe^+e^-$). We also use an effective sink term for the particle density dilution in the case of an expanding volume.

An example of some of these timescales is given in Figure 2 for our *SSC*-scenario, in which the SED is dominated by the synchrotron and inverse Compton radiation of primary injected electrons.

We consider two methods for the temporal evolution in this paper: In the *steady-state* method we keep all parameters fixed and run the system into the steady state. We use a time step of typically $10^{-2}t'_{\text{dyn}}$ and stop our evolution after $5 \times t'_{\text{dyn}}$. This truncation time only alters the results at the few percent level. This method is often applied in analytic estimates when fitting afterglow data (Sari & Esin 2001; van Eerten et al. 2010; Ryan et al. 2020). Secondly, in the *time-dependent* method we change Γ over time (see equation 8), such that the system reaches a quasi-steady state, in which the blast wave parameters evolve slowly and the system continuously catches up with the change of the blast wave parameters. This method has also been applied in a couple of works (Chiang & Dermer 1999; Pe'er & Waxman 2005; Fan et al. 2008; Petropoulou & Mastichiadis 2009; Pennanen et al. 2014; Fukushima et al. 2017). For the *time-dependent* method, we use a logarithmically growing time step of typically $10^{-2}t'_{\text{dyn}}(t)$ and start our evolution typically a few hundred steps before t .

It can be shown that in the afterglow cases both methods yield essentially $\hat{n}'_E \propto q'_E \tau'$, with τ' being

the dominant (smallest) cooling time scale, and agree up to a factor α_{corr} of order unity and a convergence term $C(t)$ (when starting from empty initial conditions $\hat{n}'_E(t'_0) = 0$):

$$\hat{n}'_E \approx q'_E \tau' \times \underbrace{\alpha_{\text{corr}}}_{\mathcal{O}(1)} \times \underbrace{C(t')}_{\rightarrow 1} \quad (11)$$

We show a comparison of a typical *SSC* scenario for the *steady-state* method and the *time-dependent* method with a constant density profile in Figure 3. It can be seen that the synchrotron components of both spectra differ only within $\mathcal{O}(1)$, with the upscattered *SSC* component for the *steady-state* method being only only twice that obtained for the *time-dependent* method (still well within an $\mathcal{O}(1)$ difference). In Appendix A we show that this is also true for the lepto-hadronic scenarios presented in our work.

We conclude from this, that within $\mathcal{O}(1)$ the *steady-state* method is a good approximation to the *time-dependent* results and that both methods lead conceptually to the same conclusions. We therefore choose the slightly faster *steady-state* method for our parameter space exploration, while we show representative scenarios obtained with the *time-dependent* method in Section 4.

3.3. Conversion to Observed Flux and Propagation Effects

We convert the comoving number density of escaping photons and neutrinos to the observed flux as follows (again up to $\mathcal{O}(1)$ and with $\mathcal{D} \approx \Gamma$):

$$EF_E \equiv E^2 \frac{d^3 N}{dE dt dA} = \frac{\Gamma^2 V' E'^2 \hat{n}'_E}{4\pi d_L^2 t'_{\text{esc}}} \quad (12)$$

Here, we define the comoving volume to be $V' = 4\pi r_*^3/\Gamma$, approximating the shell thickness to r_*/Γ , where $r_* = 4\Gamma^2 tc$. Also, we use the cosmological model from Planck Collaboration et al. (2020) to convert the representative redshift $z = 0.1$ to the luminosity distance $d_L \approx 1.5 \times 10^{27}$ cm. Lastly, we convert the comoving energy E' to the observed one via $E = \Gamma E'$.

In order to demonstrate the observability of the SEDs, we show in our figures two grey-shaded energy ranges for typical parameters. At these energies the observed flux is exponentially suppressed during the propagation. In particular, the uncertainties in the absorption model become very large and hardly allow for a reliable de-absorption. We describe the specifics of these absorption processes in the following.

Dust absorption—The low energy (optical to ultraviolet) window is limited by scattering on dust grains of uncertain size and location. For representative parameters,

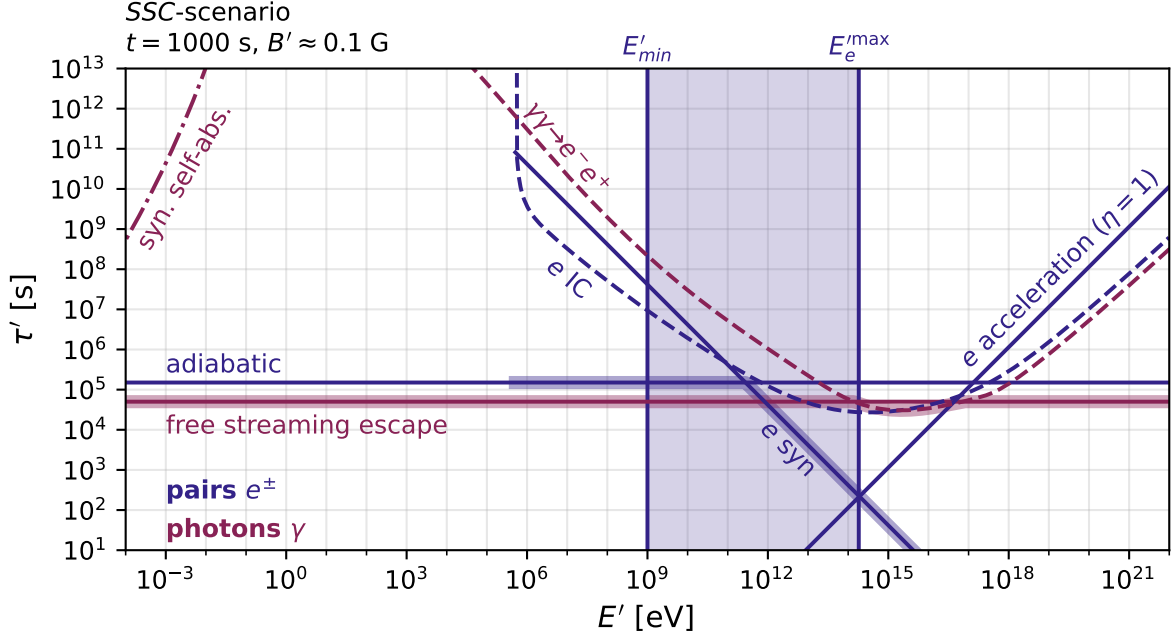


Figure 2. Comoving time scales for the *SSC*-scenario of this work (see Figure 5 for the SED and parameters used): Indigo-blue corresponds to the electrons/positrons, Bordeaux-red to photons. The plot shows the electron/positron time scales of adiabatic, synchrotron and inverse Compton (IC) scattering, as well as the acceleration time scale used to estimate the maximum energy, which combined with the minimum energy spans the power-law injection range. For photons the time scales for free-streaming escape, synchrotron self-absorption and internal annihilation into electron-positron pairs are shown. In addition, the dominant time scale at each energy is highlighted for intuition of the spectra in steady state.

the commonly used empirical model of [Pei \(1992\)](#) starts to become optically thick around 1 eV, with a large systematic uncertainty depending on the environment type chosen (Milky Way or Small/Large Magellanic Cloud) and the underlying dust size distribution.

Photo-electric absorption—With increasing energy, the absorption mechanism is taken over by the ionisation of material along the line of sight via the photo-electric effect (e.g. [Wilms et al. 2000](#)). This effect depends strongly on the amount of atoms and the metallicity, but the general scaling of the cross-section leads to an exponential suppression towards lower energies, starting from around \sim keV energies. We note that besides absorption due to the material in our own Galaxy, which can be calibrated from other known sources, typically an additional absorption component local to the emission is needed ([Willingale et al. 2013](#)), whose metallicity must be guessed.

EBL/CMB absorption—At higher energies, roughly above a few TeV for a typical redshift of 0.1, the pair production of high energy photons from the source with low energy photons of the extragalactic background light (EBL) and cosmic microwave background (CMB, rele-

vant above PeV energies) during the propagation causes again an exponential suppression. The systematic uncertainty of the EBL target field and the typical energy resolution of 10% limit our observational capabilities at higher energies (e.g. [H. E. S. S. Collaboration et al. 2017](#)).

3.4. Parameter scan and model selection

For computational speed we chose the *steady-state* method to perform a grid scan over the parameters. We summarise the parameters varied and their ranges in Table 2. We note that in order to explore extended synchrotron scenarios, we also explored the parameter space with $\eta < 1$.

Throughout the paper, we focus on the spectrum at an observation time of 1000 s and $z = 0.1$, as representative for VHE observations.

We calculate for each point of the parameter space the total photon SED. From this we select models with a flat spectrum, namely when the photon SED follows approximately a single power-law, by requiring the SED to not vary by more than a factor (in log space $\Delta \log_{10} EF_E$) in two bands with spectrally strong observations, see Figure 4: *X-ray* (from 1 keV to 100 keV), and *VHE* (from

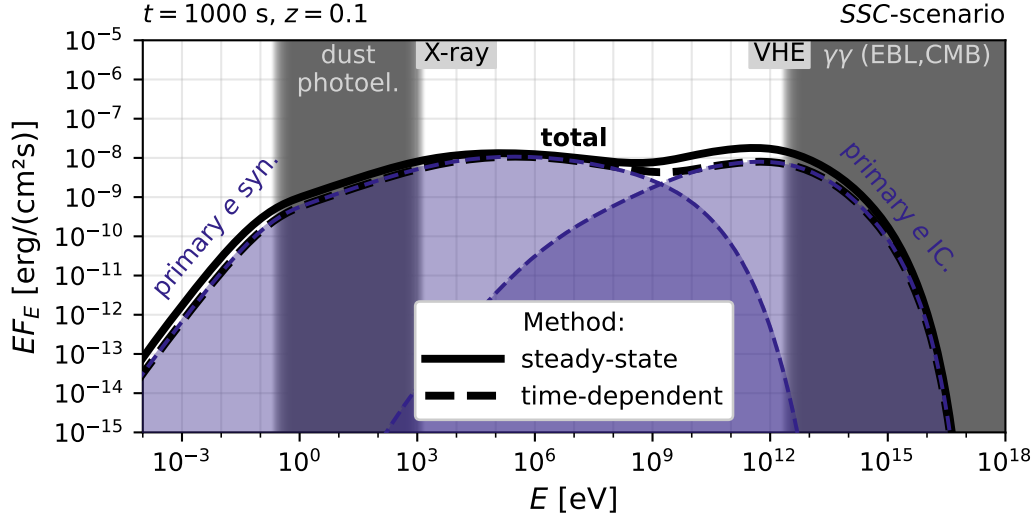


Figure 3. Comparison of time-dependent result to steady-state approximation for our *SSC* scenario. Observed energy flux as a function of observed energy for a representative parameter choice at an observed time of 1000 s. Here we show the total photon spectrum (thick black lines), with solid corresponding to the *steady-state* and dashed corresponding to the *time-dependent* method. We also indicate the contributions to the spectrum of the synchrotron (low energy component) and inverse Compton emission (high energy component) of the primary injected electrons for the *time-dependent* method. The source is placed at a representative redshift of $z = 0.1$. Furthermore, the grey shaded energy bands correspond to representative ranges of strong absorption by dust and photo-electric absorption (\sim eV-keV) and EBL absorption (\gtrsim TeV), see Section 3.3. We also sketch at the top the energy ranges (X-ray and VHE) where we filter for the solutions to be “flat”, see Section 3.4.

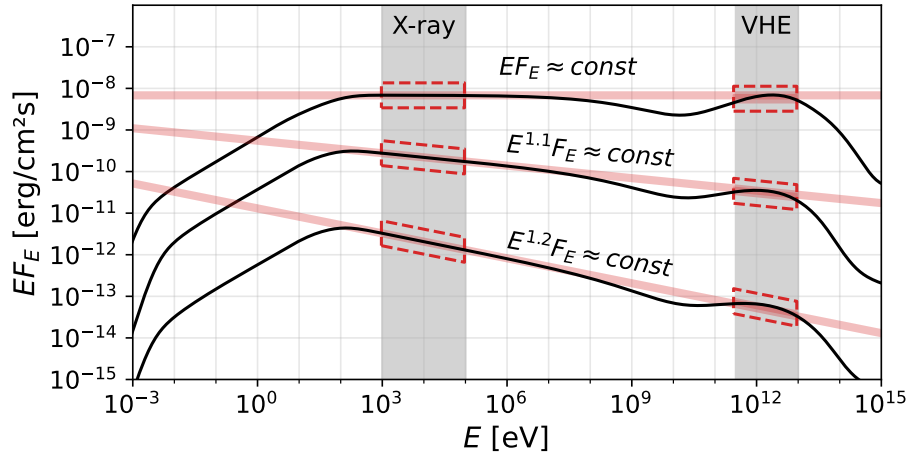


Figure 4. Conceptual sketch of the selection process for scenarios that follow our definition of “flat”. Three observed *steady-state* SEDs are shown corresponding to $E^{1+\Delta\gamma}F_E \approx const$ for $\Delta\gamma \in \{0, 0.1, 0.2\}$, corresponding to the red power-law lines. We define constant as being confined to the red dashed boxes in the two observed energy regimes $10^3 - 10^5$ eV (*X-ray*), and $10^{10.5} - 10^{13}$ eV (*VHE*), both visualised by the grey vertical bands. We emphasise the aspect ratio of 1, which allows the best visualisation of the level of flatness.

Table 2. Summary of the parameters which we varied from minimum (min.) to maximum (max.) values with a step size (step). Note that we did not explore the full parameter space for $\eta < 1$.

Parameter	min.	max.	step
$\log_{10} \Gamma$	0.7	1.7	0.25
$\log_{10} n$	-3	5	1
$\log_{10} \varepsilon_B$	-9	0	0.5
$\log_{10} \varepsilon_e$	-9	0	0.5
$\log_{10} \varepsilon_p$	-5	0	0.5
$\log_{10} E'_{\min}$	9	12	0.5
$\log_{10} \eta$	-4	4	0.5
p	2.0	2.6	0.1

0.3 TeV to 10 TeV). We motivate this factor by the typical spread, σ_γ , of photon indices, γ , from *Swift*-XRT, $\sigma_{\gamma, \text{XRT}} \approx 0.2$ (Willingale et al. 2013; Ajello et al. 2018), as well as $\sigma_{\gamma, \text{VHE}} \approx 0.3$ from GRB 190114C (MAGIC Collaboration et al. 2019a), GRB 190829A (H. E. S. S. Collaboration et al. 2021), and GRB 221009A (Cao et al. 2023). We convert this into the factor $\Delta \log_{10} EF_E$ by fully containing a power-law with slope variation within $[-\sigma/2, \sigma/2]$. We add an additional systematic uncertainty of about 0.1 and end up with a box height of about $\Delta \log_{10} EF_E \approx 0.3$, i.e. variation of the flux in each band by less than 30% of an order of magnitude. We use this criteria to select models with approximate flatness in each of the energy ranges, and require additionally that the average height ($0.5 \log_{10}(EF_E|_{\max} \times EF_E|_{\min})$) of both components is contained within a factor $10^{0.2} \approx 1.6$.

Since the observational data indicates also slightly softer power-laws than photon index 2 ($\gamma = 2$ corresponds to completely horizontal in an EF_E plot), we generalise our criteria to softer spectra by using $E^{1+\Delta\gamma} F_E$ instead. We consider three values for the tilt, $\Delta\gamma = 0$ as for GRB 190114C, $\Delta\gamma = 0.1$ as for GRB 190829A, and $\Delta\gamma = 0.2$ as for GRB 221009A. Three examples are given in a conceptual sketch in Figure 4. As all scenarios work for all three cases of $\Delta\gamma$, we choose to show for this paper only figures of the case $\Delta\gamma = 0$ and discuss the validity of the scenario for the other cases in the corresponding section.

Besides the total spectrum, we additionally track the following photon components: synchrotron and inverse Compton scattered photons from electrons from primary injection, annihilation feedback pairs ($\gamma\gamma \rightarrow e^-e^+$), proton-proton cascade secondaries, photo-pion cascade secondaries and pairs from the Bethe-Heitler process, as well as from protons, pions, and muons, and also the photons from the decay of neutral pions produced in

proton-proton and photo-pion production. More precisely, we co-evolve (without feedback into the main solution) the transport equation of secondaries using only the source term from a certain channel from the list above (in combination with the sink and cooling terms based on the main solution). Based on this we can classify the type of solution, by checking which component contributes most to the energy-integrated flux in the each of the bands. For example an *SSC*-scenario would correspond to the primary injected electron synchrotron component dominating the *X-ray* band, whereas the inverse Compton component of the same particles dominates the *VHE* band. We note that as soon as the radiation from the cascade electrons contributes significantly, also the radiation of the pairs from photon-annihilation becomes similarly strong and a classification via a dominant component is hard to make.

4. RESULTS

Following our parameter space scan and model selection (Section 3.4), we find five families of scenarios with the required flat SED behaviour. For these, we find four photon emission channels to be dominant:

1. synchrotron radiation of primary injected electrons, relevant for all scenarios
2. inverse Compton up-scattered synchrotron radiation of primary injected electrons
3. proton-proton induced cascade emission: π^0 decay photons at high energies, synchrotron radiation of secondary electrons/positrons at low energies
4. photo-pion induced cascade emission, i.e. synchrotron radiation of secondary electrons/positrons

This leads to five conceptually different types of flat scenarios: *SSC*, *Extended-syn*, *Proton-syn*, *pp-cascade*, and *p γ -cascade*. We summarise the properties, advantages, and problems of these scenarios in Table 3, and discuss a representative parameter set for each scenario in the following sections.

4.1. The *SSC* scenario

In the *SSC* scenario the photon emission in our *X-ray* and *VHE* bands are dominated by the synchrotron and inverse Compton components, respectively, of the primary injected electrons. We show in Figure 5 the observed SED for a representative set of parameters. The figure is similar to Figure 3, though we focus here on the *time-dependent* method. We refer to Figure 2 for a plot of the corresponding time scales.

Table 3. Summary table of the discussed scenarios

Name	Low E Comp.	High E Comp.	Specifications	Advantages	Limitations
<i>SSC</i> (Section 4.1)	primary electron syn.	primary electron IC	- leptonic dominated - slow cooling electrons - low E'_{\min} - efficient acceleration ($\eta \sim 1$) - moderate n, Γ	- bright	KN suppression → VHE slope → fine-tuned height ratio
<i>Extended-syn</i> (Section 4.2)	primary electron syn.		- leptonic dominated - extreme acceleration ($\eta \ll 1$) - higher E'_{\min} (less IC targets) - moderate n, Γ	- bright - directly yields single power-law	- requires $\eta \ll 1$ (challenging for 1 zone)
<i>Proton-syn</i> (Section 4.3)	primary electron syn.	proton syn.	- lepto-hadronic - high n, Γ - efficient acceleration ($\eta \sim 1$) - moderate baryonic loading ($\varepsilon_p/\varepsilon_e \sim 10^2$)	- bright	- p -syn. component at exp. cut-off (fine-tuning) → flux level → peak energy → shape of UHE p cut-off
<i>pp-cascade</i> (Section 4.4)	primary electron syn.	pp created π^0 -decay	- lepto-hadronic - very high n, Γ - extreme baryonic loading ($\varepsilon_p/\varepsilon_e \sim 10^6$)	- flat VHE comp. extending beyond 10 TeV	- dim
<i>$p\gamma$-cascade</i> (Section 4.5)	primary electron syn.	$p\gamma$ created electron (e^\pm) syn.	- lepto-hadronic - extreme n, Γ - high baryonic loading ($\varepsilon_p/\varepsilon_e \sim 10^4$)	- bright	- extreme energy requirements

Figure 5 shows the total photon SED and the contributions from the different radiation channels. In indigo-blue the synchrotron (dominant at low energies) and inverse Compton up-scattered synchrotron emission (at high energies) of the primary shock-accelerated electrons are shown. The subdominant purple lines show the contribution of the secondary pairs from photon annihilation ($\gamma\gamma \rightarrow e^-e^+$), more specifically their synchrotron emission and their inverse Compton emission (with the total photon spectrum as a target).

We note that the parameters in the table next to the plot are rather typical for GRB modelling. The choice $\varepsilon_p = 0$ is for simplicity and we note that even for $\varepsilon_p = 1$ the hadronic components stay subdominant in the regime of the parameter space occupied by the *SSC* scenario.

In order to understand the photon spectrum it is necessary to understand the shape of the primary injected electrons. For this, in the steady-state approximation $\hat{n}'_E \sim q'_E \tau'$ (cf. eq. 11), the dominant time scales and the injection energy range in Figure 2 (shaded in indigo-blue) are instructive. Three regimes emerge, which is also known as slow cooling case, with cooled electron spectral indices ($\hat{n}'_E \propto E'^{-s}$):

1. **adiabatic cooling tail:** $E'_e < E'_{\min}$ with $s = 1$

2. **adiabatic cooling regime:**

$$E'_{\min} < E'_e \lesssim 3 \times 10^{11} \text{ eV with } s \approx s_{\text{inj}}$$

3. **synchrotron cooling regime:**

$$3 \times 10^{11} \text{ eV} \lesssim E'_e < E'^{\text{max}}_e \text{ with } s \approx s_{\text{inj}} + 1$$

The resulting synchrotron photon spectrum resembles the electron spectrum with these critical energies in the electron spectrum mapping to

$$E'^{\text{syn}}_\gamma \approx \frac{B'}{B_e^{\text{crit}}} \frac{E_e'^2}{m_e c^2}, \quad (13)$$

in the photon spectrum. Here, $B_e^{\text{crit}} \approx 4 \times 10^{13} \text{ G}$ is the critical magnetic field for electrons, m_e is the electron mass, and c the speed of light. Thus, the cooling break at $E'_e \approx 3 \times 10^{11} \text{ eV}$ maps to an observed photon energy of

$$E_\gamma^{\text{cb}} \approx \Gamma \frac{B'}{B_e^{\text{crit}}} \frac{E_e'^2}{m_e c^2} \approx 3 \times 10^4 \text{ eV}. \quad (14)$$

Additionally, the slopes of the electron spectra get stretched ($\Delta \ln E'^{\text{syn}}_\gamma = 2\Delta \ln E'_e$) and one finds for the photon indices (defined as $EF_E E^{2-\gamma}$): $\gamma = (s_{\text{inj}} + 1)/2 \approx 1.7$ for $E'_e < E_\gamma^{\text{cb}}$ and $\gamma = (s_{\text{inj}} + 2)/2 \approx 2.2$ for $E'_e > E_\gamma^{\text{cb}}$. This results in a roughly flat synchrotron spectrum in the *X-ray* band. The choice of $\eta = 1$ leads to a maximum synchrotron photon energy $E_\gamma^{\text{syn,max}} \approx$

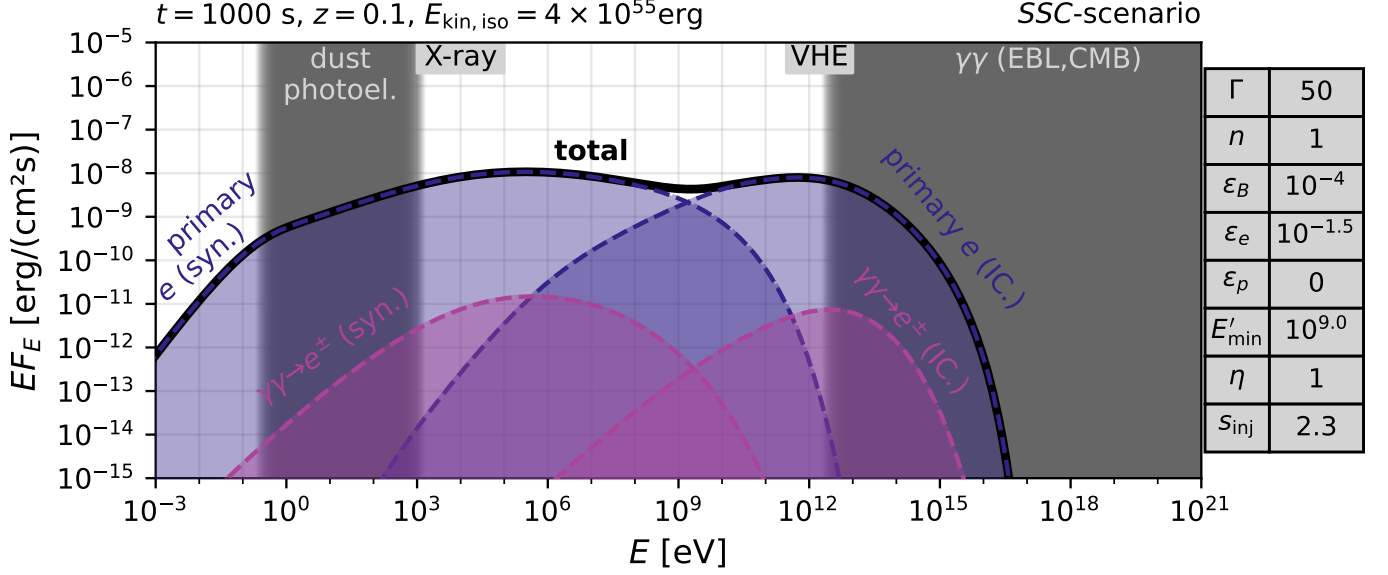


Figure 5. SSC scenario (time-dependent method): Observed energy flux as a function of observed energy for a representative parameter choice (see table at the side with symbols as in text, note n in cm^{-3} and E'_{\min} in eV) at an observed time of $t = 1000$ s. The source is placed at a redshift of $z = 0.1$. Shown here are the total photon spectrum and its contributions as described next to the dashed lines: the synchrotron and inverse Compton emission of the primary injected electrons, and the synchrotron and inverse Compton emission of the electron/positron pairs created by annihilated photons ($\gamma\gamma \rightarrow e^-e^+$). See Figure 3 for a more detailed description of the SED plots and Figure 2 for the corresponding time scales.

$\Gamma E_{\gamma}^{\text{syn, burnoff}} \approx 10$ GeV (here $E_{\gamma}^{\text{syn, burnoff}} \approx 150$ MeV is the (comoving) burn-off limit; see, e.g., Khangulyan et al. 2021, for a detailed discussion).

The IC spectrum can be understood in a similar way to the synchrotron spectrum, although the break features and the power-law slopes are washed out stronger through the broader kernel from the synchrotron target, which extends over many (5-10) orders of magnitude in energy. Additionally, for observed energies in/above the VHE band, the Klein-Nishina effects to the IC kernel have to be taken into account (note also the discussion of the validity of this approximation in the supplementary materials of H. E. S. S. Collaboration et al. (2021), Equation S21):

$$E_{\gamma}^{\text{KN}} \approx \Gamma^2 \frac{(m_e c^2)^2}{E_{\gamma}^t} \approx 1 \text{ TeV} \left(\frac{\Gamma}{50} \right)^2 \left(\frac{E_{\gamma}^t}{10^3 \text{ eV}} \right), \quad (15)$$

with photon target energy E_{γ}^t . Here we have assumed that the electron gives most of its energy to the up-scattered photon. The suppression of the IC cross-section above these energies requires the existence of a target photon spectrum extending *at least down to* energies E_{γ}^t in order to maintain flatness in the IC component. In our SSC scenario the spectrum starts to decrease, however, slowly already below the X-ray band, as also typical for the observational picture (see, e.g.,

Figure 1). This leads to a washed-out turnover at TeV energies and has two limiting implications in light of flat photon spectra extending to even higher energies.

First, in the extreme Klein-Nishina regime ($E_e' E_{\gamma}' \gg m_e^2 c^4 \approx 3 \times 10^{11} \text{ eV}^2$) the observed photon index is $\gamma = s_{\text{inj}} + 1 \approx 3.3$ (adiabatically cooled electrons) or $\gamma = s_{\text{inj}} + 2 \approx 4.3$ (synchrotron-cooled electrons). This is in conflict with the much harder observed values of $\gamma \approx 2 - 2.2$. The broad target spectrum can alter the slope slightly, but does not resolve this conflict.

Secondly, the height (i.e. energy density) of the IC component no longer scales with the energy density in the electrons, but sits below this level. This implies that the well-known result for the height ratio of the synchrotron (u'_{esyn}) and the IC (u'_{eSSC}) component no longer scale as $u'_{\text{esyn}}/u'_{\text{eSSC}} \propto \epsilon_B/\epsilon_e$. Thus an equal height ratio requires a special choice of ϵ_B and ϵ_e .

The time scale plot in Figure 2 shows two other interesting aspects. First, the IC cooling time scale for the electrons is sufficiently large so as to be safely negligible. Indeed, at the cooling break all three (IC, synchrotron, adiabatic) time scales are at the same level. This is linked to the fact that the energy density in both photon components, synchrotron and IC, is tuned to a similar value. For electron spectra with spectral index between 2 and 3, the power ($\propto E_e'^2$ for synchrotron and IC) sits mainly at the cooling break energy. On the other hand,

the cooling time is linked to exactly the power lost by an electron. Thus, a comparable energy density will always result in roughly comparable cooling times, such as that in Figure 2 (see also the discussion in Appendix A of Klinger et al. 2023a).

The second interesting aspect is the effect of photon annihilation into electron/positron pairs. Its importance can be read off from the dashed Bordeaux-red curve (also for the photons $\hat{n}'_E \approx q'_E \tau'$), showing that for this scenario the effect would be only very small around energies of 1–10 PeV. For this set of parameters, this is just above the maximum energy of injected electrons and not relevant for their SED. However, stronger $\gamma\gamma \rightarrow e^+e^-$ absorption can lead to additional softening in the photon spectrum.

We note that all the above discussed aspects also qualitatively hold for the case of slightly tilted spectra ($\Delta\gamma \gtrsim 0$).

We conclude that the *SSC* scenario allows for similar energy flux levels in the *X-ray* and *VHE* bands. However, a more detailed inspection of the spectral shape reveals significant curvature, especially at the highest energies (> 1 TeV) due to the Klein-Nishina effects. Additionally, we find *SSC* scenarios to exist only for reasonably large values of $\Gamma \gtrsim 10$ (compare eq. 15) and $\eta \approx 1$ (to fill up the GeV range with synchrotron photons). Both points, curvature and large Γ , create conflicts for the cases of GRB 190829A with a low Γ (H. E. S. S. Collaboration et al. 2021) and GRB 221009A extending with an unbroken power-law to at least 10 TeV (Cao et al. 2023).

4.2. The Extended-syn scenario

Before turning to scenarios with dominant hadronic components, we first discuss the conceptually simple idea of a single electron synchrotron component extending from the *X-ray* to the *VHE* band.

Figure 6 combines the SED and the time scales for a representative set of parameters. We note that we choose for simplicity $\varepsilon_p = 0$, but this does not affect our conclusions.

The SED can be understood in a similar manner to the *SSC* scenario. In the *Extended-syn* scenario, slightly larger values of ε_B (which places $E_\gamma^{\text{cb}} \lesssim 10^3$ eV for flatness in the *X-ray* band) and E'_{min} (which reduces the IC component) are required. From the time scales plot we can see that this leads to all electrons being cooled (no adiabatically cooled regime, compare to regime 2 of the *SSC* scenario). Furthermore, the IC target for $E_\gamma^{\text{t}} < 10^3$ eV is reduced, leading to a subdominant SSC component and an almost constant IC cooling time for 10^{10} eV $\lesssim E'_e \lesssim 10^{16}$ eV.

Most crucial is, however, the parameter $\eta \ll 1$, which increases the maximum synchrotron energy into the *VHE* band. This can be seen as follows: Particle acceleration requires an electric field \mathcal{E}' , such that in the simplest case the relativistic particle energy $E'_{\text{particle}} \approx e\mathcal{E}'ct'_{\text{acc}}$ after an acceleration time t'_{acc} . However, in ideal magneto-hydrodynamic (MHD) plasma currents short out these electric fields on a much shorter time scale. Instead one can consider a moving magnetic field resulting in an effective electric field with some efficiency factor depending on the details of the setup like the geometry. We thus define here:

$$t'_{\text{acc}} = \frac{E'}{e\mathcal{E}'c} = \eta \frac{E'}{eB'c} = \eta \frac{r_L}{c}. \quad (16)$$

η can thus be interpreted as the ratio of the magnetic and effective electric field or the number of Larmor radii r_L needed to increase the particle energy by an e-fold. Thus, in earlier works the parameter η was rather expected to be $\gg 1$ (e.g. recently Huang et al. 2022).

A value of $\eta \ll 1$ in the one-zone approximation would require that the ideal MHD conditions are no longer valid, such as in the case of reconnecting field lines (for details see Khangulyan et al. 2021). An alternative explanation is that η acts only as an effective parameter for one-zone modelling. In this case, it incorporates the effect of two (or multi) zone models with different magnetic field strengths; see, e.g., Khangulyan et al. (2021). For example, a weak magnetic field is filling up most of the space and dictates the particle acceleration rate, whilst a strong magnetic field in tiny blob regions yields catastrophic energy losses and produces the observed synchrotron radiation.

Obviously, all these results are also true for the case of slightly tilted spectra ($\Delta\gamma \gtrsim 0$).

We conclude that the *Extended-syn* scenario can produce flat, extended SEDs in a straight-forward manner, however the necessary assumption of $\eta \ll 1$ requires careful explanation going beyond the scope of this paper.

4.3. The proton synchrotron scenario

Another idea recently suggested to explain the *VHE* band photons is the *Proton-syn* scenario (e.g. Isravel et al. 2023b,a). In this case the proton synchrotron emission dominates the *VHE* band, whereas the *X-ray* band is dominated by the electron synchrotron component. We show the SED and the corresponding time scales for a representative parameter set in Figure 7. As an example, we also added for this scenario the comoving particle energy distributions in Appendix B in Figure 11.

The SED shows, besides the proton synchrotron component (olive-green, including an IC contribution rel-

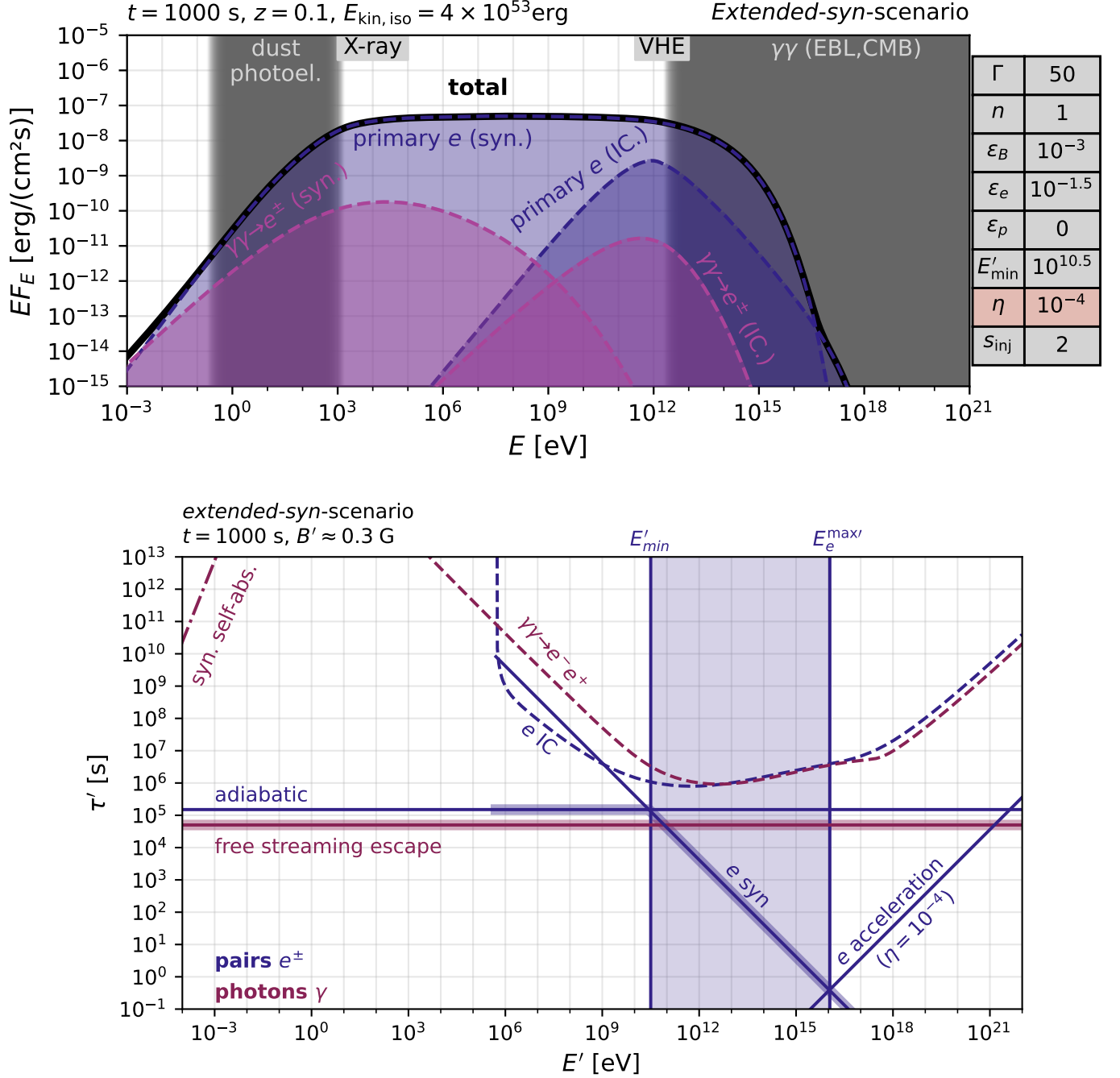


Figure 6. *Extended-syn* scenario (time-dependent method) — **Top:** Observed energy flux as a function of observed energy for a representative parameter choice (n in cm⁻³ and E'_{min} in eV). We highlighted the parameter η due to its extreme value. For a detailed description of the figure see Figure 5. **Bottom:** Comoving time scales similar to Figure 2.

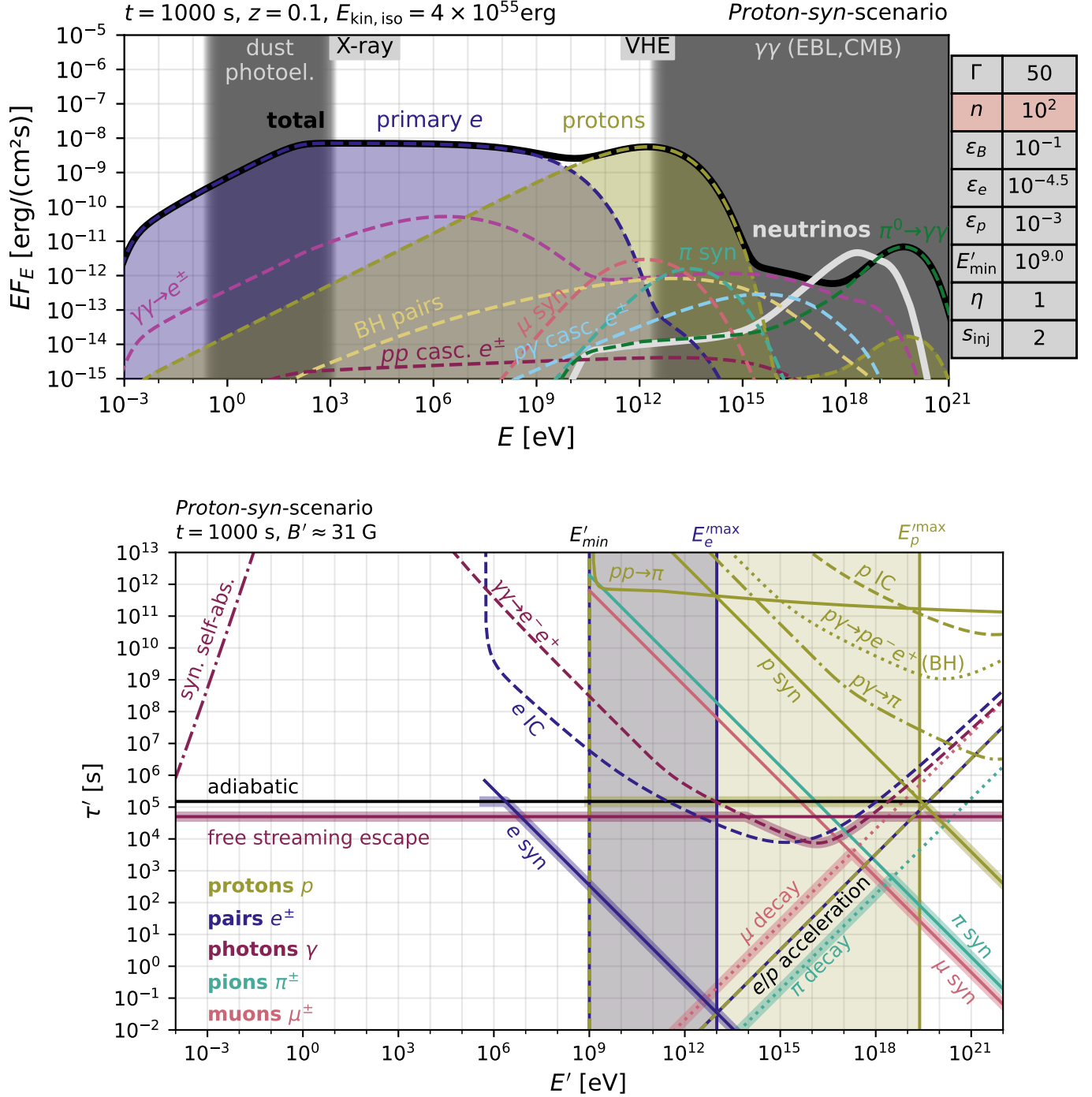


Figure 7. Proton-syn scenario (time-dependent method) — **Top:** Observed energy flux as a function of observed energy for a representative parameter choice (for a detailed description of the figure see Figure 5, note n in cm⁻³ and E'_{min} in eV). Additionally all the hadronic contributions are shown: proton synchrotron and inverse Compton (protons); synchrotron and inverse Compton from the pairs created in the Bethe-Heitler process (BH pairs), photo-pion cascade ($p\gamma$ casc. e^\pm) and proton-proton cascade (pp casc. e^\pm); synchrotron emission from charged pions (π syn) and muons (μ syn) and the photons from neutral pion decays ($\pi^0 \rightarrow \gamma\gamma$). We also show the total flux of neutrinos of all flavours in light grey (neutrinos). We highlighted the density n due to its extreme value.

Bottom: Comoving time scales: Olive-green corresponds to protons, indigo-blue to electrons/positrons, Bordeaux-red to photons, cyan to charged pions and pink to muons. The plot shows the time scales of adiabatic (black, same for all charged particles), synchrotron ($e/p/\pi/\mu$ syn), inverse Compton (e/p IC) scattering, inelastic proton-proton collisions ($pp \rightarrow \pi$), photo-pion production ($p\gamma \rightarrow \pi$), Bethe-Heitler process ($p\gamma \rightarrow pe^-e^+$) and charged pion and muon decay. It also shows the acceleration time scale used to estimate the maximum energy for proton and electrons, which combined with the minimum energy spans the power-law injection range shaded in dark-blue/olive. For the photons the time scales for free-streaming escape, synchrotron self-absorption and internal annihilation into electron-positron pairs ($\gamma\gamma \rightarrow e^-e^+$) are shown. In addition, the dominant time scale at each energy is highlighted for each species for intuition of the spectra in steady state.

evant only above $E_\gamma \approx 10^{16}$ eV), the other hadronic components. However, these other components are subdominant below $E_\gamma < 10^{15}$ eV. Also, the time scales plot shows the relevant time scales for protons, pions and muons.

We briefly discuss these different SED components. The primary electron synchrotron spectrum can be understood in analogy to the *SSC* scenario in Section 4.1. In the *Proton-syn* scenario the magnetic field is stronger, such that the time scale plot shows a fast cooling case, with two relevant regimes (electron spectral index $\hat{n}'_E \propto E_e'^{-s}$):

1. **synchrotron cooling tail:**

$$E'_e < E'_{\min} \text{ with } s \approx 2$$

2. **synchrotron cooling regime:**

$$E'_e \geq E'_{\min} \text{ with } s \approx s_{\text{inj}} + 1$$

This results in the two power-law regimes below and above $E_\gamma \approx 10^2$ eV with photon indices $\gamma = 1.5$ (below) and $\gamma = (s_{\text{inj}} + 2)/2 = 2$ (above). The other break at $E_\gamma \approx 3 \times 10^{-3}$ eV originates from synchrotron self-absorption, as can be seen from the photon time scales. The maximum energy of the electron synchrotron component is, as in the *SSC* scenario, at around 10 GeV corresponding to $\eta = 1$.

The proton synchrotron component can be understood analogously by replacing the mass $m_e \rightarrow m_p$ and thus also the critical magnetic field $B_e^{\text{crit}} = m_e^2 c^3 / e \hbar \rightarrow B_p^{\text{crit}} \approx B_e^{\text{crit}} (m_p / m_e)^2 \approx 1.5 \times 10^{20}$ G. In the quasi-steady state approximation, the proton cooling is dominated by adiabatic cooling for all injected energies, leading to a single power-law spectrum with the original injected spectral index and an exponential cut-off at $E_p^{\text{max}} \approx 2 \times 10^{19}$ eV. The resulting synchrotron spectrum therefore has the photon index $\gamma = (s_{\text{inj}} + 1)/2 = 1.5$ and a cut-off position at

$$E_\gamma^{\text{syn,max,p}} \approx \Gamma \frac{B}{B_p^{\text{crit}}} \frac{(E_p^{\text{max}})^2}{m_p c^2} \approx 10^{13} \text{ eV}, \quad (17)$$

in agreement with the peak energy in Figure 7. The presence of UHE protons requires comparably strong magnetic fields (here ≈ 30 G), leading to either large upstream density requirements (highlighted here in the table), Lorentz factors, or values of ε_B (which is bound to be smaller than 1). This large magnetic field is also needed to cool the primary electrons to yield a flat synchrotron spectrum down to the *X-ray* band.

Besides the synchrotron radiation, the UHE protons also induce a secondary cascade via photo-pion production on the target field provided by the electron

synchrotron component. Approximating that the neutral pions obtain about 20% of the maximum proton energy and then decay into two photons with half of that energy results in the green $\pi^0 \rightarrow \gamma\gamma$ peak at $E_\gamma^{\pi^0 \rightarrow \gamma\gamma} \approx \Gamma E_p^{\text{max}} / 10 \approx 10^{20}$ eV.

The charged pions predominantly decay into muons and neutrinos, as can be seen from the pion synchrotron cooling curve only being dominant above about 3×10^{18} eV. The resulting muons decay slower than the pions, such that they are affected stronger by synchrotron cooling, roughly by one order of magnitude down to energies of $E'_\mu \approx 10^{17}$ eV (compare dominant time scale highlighted in pink). They subsequently decay further into neutrinos with a complex spectral shape consisting of a plateau, a peak and a cut-off at E_ν^{max} . We can estimate roughly $E_\nu^{\text{max}} \approx \Gamma E_p^{\text{max}} / 20 \approx 10^{19}$ eV and a peak position originating from the peak in the muon spectrum at $E_\nu \approx \Gamma \times 10^{17}$ eV $\approx 3 \times 10^{18}$ eV. The low energy plateau is dominated by neutrinos from *pp*-interactions, with the flat shape due to the flat proton spectrum. We note that the neutrino flux is below the current and planned detector limits, see Appendix C for details.

The synchrotron radiation for both, charged pions and muons, is shown in the SED too. We can estimate the peak frequencies from the peak positions of the charged pion and muon spectra, at $E_\pi^{\text{peak}} \approx 3 \times 10^{18}$ eV and $E_\mu^{\text{peak}} \approx 10^{17}$ eV, similar to the proton case by replacing $B_\pi^{\text{crit}} \approx 3 \times 10^{18}$ G, $B_\mu^{\text{crit}} \approx 2 \times 10^{18}$ G. This is in good agreement with the pion synchrotron peak at around $E_\gamma^{\text{syn,max},\pi} \approx 3 \times 10^{13}$ eV and the slightly cooling-broadened muon peak observed at $10^{12} - 10^{13}$ eV.

Furthermore, the muons also decay into secondary electrons and positrons, whose synchrotron and inverse Compton emission is also shown in the SED ($p\gamma$ casc. e^\pm , light-blue). This component follows qualitatively the shape of the cooled muons, leading to a relevant contribution in the range of $E_\gamma \approx 10^{15} - 10^{18}$ eV. As can be seen from the photon loss time scale for $\gamma\gamma \rightarrow e^- e^+$ pair annihilation, at these energies the feedback into secondary pairs is very efficient, triggering the electromagnetic cascade that dominates the photon spectrum in this energy range ($\gamma\gamma \rightarrow e^\pm$, purple). We can also see that the pair annihilation does not affect the proton synchrotron component sufficiently to impact the shape in the *VHE* band. Inspecting the $\gamma\gamma \rightarrow e^- e^+$ induced cascade emission curve in the SED we can additionally see two other features. The broad peak in the observed MeV range is due to the synchrotron emission radiated by secondary pairs, produced through $\gamma\gamma$ annihilation of primary electron synchrotron photons with the proton synchrotron photons. At the highest energies (up

to $E_\gamma \approx 10^{20}$ eV), the $\gamma\gamma \rightarrow e^-e^+$ cascade is instead triggered by the $\pi^0 \rightarrow \gamma\gamma$ peak, and suppressed in the quantum synchrotron regime (*Klein-Nishina* cut-off for synchrotron radiation).

Finally, we also see a subdominant component of the secondary electrons from the pp induced cascade, which follows the shape of the parent proton spectrum (power-law with spectral index 2 in this case).

In light of our search for extended and flat spectra, we find that by tweaking the parameters (mainly $\Gamma, n, \varepsilon_B, \varepsilon_p$) towards high magnetic fields (here ≈ 30 G), the proton synchrotron component can be fine-tuned to ensure that the total SED is approximately flat up into the *VHE* band. However, similar to the *SSC* scenario, the proton synchrotron component is not genuinely creating flat spectra in the *VHE* band due to the presence of the exponential cut-off. This implies that a certain level of fine tuning is required in order to ensure that the energy of the peak, as well as its flux level, are both at the right positions. It should also be noted that the proton cut-off is likely more complex than in our simplified exponential cut-off due to the transition from adiabatic cooling to free streaming escape.

We additionally note that this scenario is able to create flat spectra in our slightly tilted cases ($\Delta\gamma \gtrsim 0$) too.

We conclude that in a situation of large magnetic fields and efficient proton acceleration, the proton synchrotron component can dominate the emission, but its exponential cut-off struggles to genuinely explain the observed flatness of the power-law spectra.

4.4. The pp cascade scenario

In this scenario, the *VHE* band is dominated by the π^0 decays from pp interactions, whereas the *X-ray* band is dominated by the synchrotron radiation from primary electrons. Figure 8 shows the SED and time scale for a representative set of parameters. For the sake of comparability, the y-range (energy flux) is kept the same in the figures of all scenarios. This helps to highlight a limitation of this scenario. Despite the rather high upstream density of $n = 10^3 \text{ cm}^{-3}$ (highlighted next to plot), the total flux level is noted to be rather dim⁴.

At low energies, the primary electron synchrotron component is in the slow cooling regime and can be understood as in the *SSC* scenario. The proton synchrotron component in this scenario is subdominant, peaking at around $E_\gamma^{\text{syn,max},p} \approx 10^6$ eV. This is consis-

tent with the *Proton-syn* scenario, where the magnetic field is higher and therefore the adiabatic-cooling limited maximum energy too (note also that $\eta = 3$).

More relevant in this scenario are the components from the pp -cascade. In particular, the emission observed above ≈ 1 GeV originates from the decay of the produced, neutral pions. The cut-on energy is related to the lowest energy protons and limited to the threshold at the pion mass $E_\gamma^{\pi^0, \text{cut-on}} \approx \Gamma m_{\pi^0} c^2 / 2 \approx 10^9$ eV. Since the protons cool dominantly adiabatically, their flat spectrum yields also a flat photon spectrum above the cut-on energy. Especially, this extends up to $E_\gamma^{\pi^0, \text{max}} \approx \Gamma E_p^{\text{max}} / 10 \approx 10^{18}$ eV. This is an interesting feature in the context of the recent flat *VHE* observations.

It is worth noting that pp -interactions are less efficient compared to the electron synchrotron mechanism, such that a large baryonic loading $\varepsilon_p / \varepsilon_e \approx 10^6$ (highlighted next to plot) is needed for both components to be at a similar energy flux level. Our tilted criterion ($\Delta\gamma > 0$, see Figure 4) only mildly relaxes this extreme requirement. We note that very large baryonic loadings $\gtrsim 10^4$ are frequently considered in the modelling of AGN blazars in the context of neutrino observations; see, e.g., Gao et al. (2019); Rodrigues et al. (2021).

In addition, the synchrotron radiation from secondary electrons/positrons generated from the pp -cascade, is shown in the SED figure ($pp\text{-casc. } e^\pm$). In principle the secondary injection follows the parent proton spectral index, such that efficient electron cooling (see time scales) leads to a flat synchrotron spectrum. The efficient cooling also distributes the energy over a large range of energies (> 10 orders of magnitude), making this component subdominant.

Lastly, the secondary neutrino flux follows approximately the parent proton spectrum too, similar to that of the other secondaries, with a slightly lower maximum energy. The neutrino flux is below detection limits (see Appendix C).

We also note, that the extreme value of $\varepsilon_p = 1$, relevant for the brightness of this scenario, is already in conflict with the assumption that the non-thermal proton pressure downstream is negligible in the hydrodynamic shock approximation.

Furthermore, we point out that the density of material in the vicinity around GRB explosions is hard to constrain observationally. However for environments with high star formation, such as molecular clouds, densities of 10^3 cm^{-3} are not uncommon.

We conclude that a combination of the primary electron synchrotron and the pp -cascade induced $\pi^0 \rightarrow \gamma\gamma$ emission can yield flat photon spectra, when extremely

⁴ This is consistent with the intuition that pp interactions are typically important in extended sources, such as star-forming/burst galaxies or galaxy clusters (e.g. Senno et al. 2015; Yuan et al. 2018).

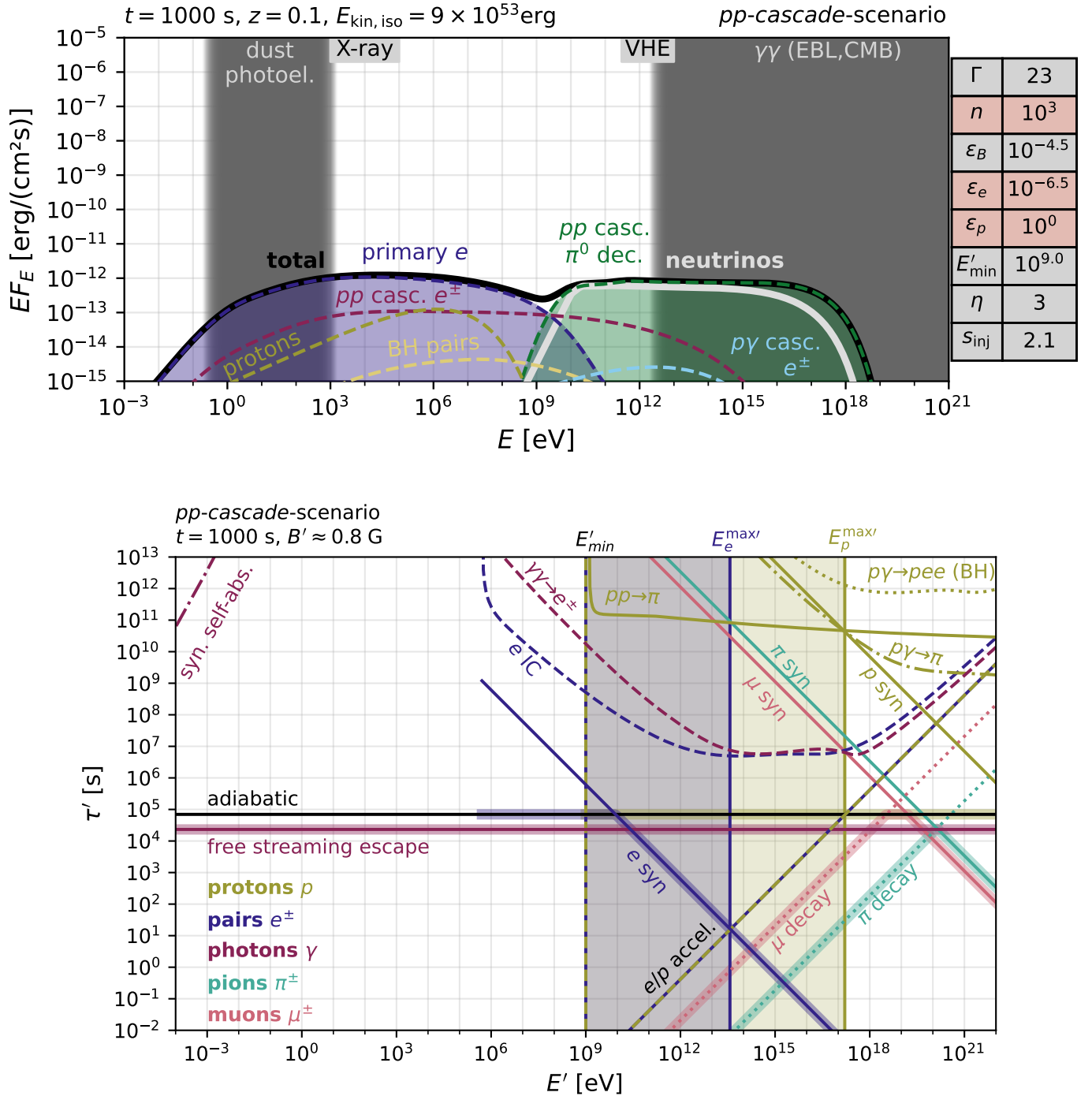


Figure 8. *pp-cascade scenario (time-dependent method)* — **Top:** Observed energy flux as a function of observed energy for a representative parameter choice (for a detailed description of the figure see Figure 5 and 7, note n in cm^{-3} and E'_{\min} in eV). We highlighted the density n and the parameters $\varepsilon_e, \varepsilon_p$ due to their extreme combination of values. **Bottom:** Comoving time scales (for a detailed description of the figure see Figure 2 and 7).

large values of the baryonic loading ($\varepsilon_p/\varepsilon_e \approx 10^6$) and high densities are chosen. We highlight the natural emergence of a hard spectral component extending significantly beyond TeV energies allowed by this scenario, despite the comparably dim energy fluxes.

4.5. The $p\gamma$ cascade scenario

We finally show a scenario in which the photo-pion induced cascade synchrotron emission dominates the *VHE* band. The SED and time scales are shown in Figure 9.

Again the *X-ray* band is dominated by synchrotron emission from primary injected electrons, and the cooling regimes can be understood analogously to the *Extended-syn* scenario.

The SED at higher energies is dominated by the different emission components from the $p\gamma$ -cascade. They can be understood in a similar manner to the *Proton-syn* scenario. Also here, the peak energy of the neutral pion bump can be estimated to $E_{\gamma^0 \rightarrow \gamma\gamma} \approx \Gamma E_p^{\text{max}}/10 \approx 10^{19}$ eV. Due to the rather abrupt cut-on of the fast cooling synchrotron spectrum at $E_\gamma \approx 3 \times 10^2$ eV, the $\pi^0 \rightarrow \gamma\gamma$ bump does not trigger an efficient pair annihilation cascade.

Different to the *Proton-syn* scenario, here the lower magnetic field $B' \approx 1$ G results in the secondary muons and pions decaying before cooling significantly via synchrotron emission. We can understand the shape of the resulting $p\gamma$ cascade electron (positron) synchrotron component by simple scaling arguments. In the δ -approximation, the source term of pions roughly scales as $q'_{E,\pi} \propto q'_{E,p} t'_{\text{adi}}/t'_{p\gamma} \propto (E'_\pi)^{-s_{\text{inj}}+1}$, since $t'_{p\gamma} \propto 1/E'_p$ in the relevant energies (flat photon target, compare time scale plot). The pions and muons directly decay, such that the electron spectrum is approximately $\hat{n}'_{E,e} \propto t'_{\text{syn}} \hat{n}'_{E,\pi}/t'_{\pi\text{-dec}} \propto (E'_e)^{-s_{\text{inj}}}$, since the electrons are fast cooling. This results in the rising synchrotron photon source term with photon index $\gamma = (s_{\text{inj}}+1)/2 = 1.5$ in this scenario. As can be seen from the photon time scale, the energy-independent free streaming escape dominates up to $E'_\gamma \approx 10^{12}$ eV, with a break feature from the transition to $\gamma\gamma \rightarrow e^\pm$ annihilation. This feature imprints itself as a softening in the photon spectrum above $E_\gamma \approx 10^{13}$ eV, which results in the effective flat photon SED above TeV energies. This annihilation subsequently triggers an electromagnetic cascade ($\gamma\gamma \rightarrow e^\pm$ component in SED plot), which propagates with an approximately flat spectrum down to at least the MeV energy range.

Due to the high downstream density, the sub-dominant radiating particle components (protons, pions and muons), show besides their synchrotron peaks, an additional (sub-dominant) IC peak.

Compared to the other scenarios, the neutrino flux in this scenario is highest, although only touching the sensitivity of future instruments (see Appendix C for further details).

We note that similar parameters can be found to yield slightly softer spectra fulfilling our selection criteria for $\Delta\gamma \gtrsim 0$.

The difference in the $p\gamma$ -cascade scenario compared to the others is, in particular, the comparatively large energy requirement, coming from the combination of high circum-burst densities, and high Γ . We discuss the feasibility of these conditions in Section 5.2. We note that the extreme assumption of $\varepsilon_p = 1$ (also highlighted next to the plot) is already too high to be compatible with a purely hydrodynamical shock. Additionally, the baryonic loading, $\varepsilon_p/\varepsilon_e = 10^{4.5}$, is rather extreme, but comparable to that considered in AGN blazar models (see earlier discussion for pp -cascade scenario). This is required to compensate the low $p\gamma$ efficiency, such that the proton population gives only a small fraction of the energy to the pion population (not calorimetric).

We conclude that this scenario can result in a flat spectrum extending up to energies \gg TeV, but is energetically more challenging than the other scenarios that we found.

5. DISCUSSION

5.1. Limitations of our Results

In this paper, we seek to reproduce the observed spectral properties of GRB afterglows, namely flat (i.e. $\gamma \approx 2 - 2.2$) spectra in our *X-ray* (keV) and *VHE* (TeV) energy bands, that additionally connect to a single power-law, in a single-zone, lepto-hadronic, relativistic-shock model. We provide a robust and comprehensive, conceptual answer to this question that is based on a large parameter scan. We find five different families of solutions. However, none of these solutions appears to satisfy all the above model selection criteria in a convincing and exclusive manner. In the following, we discuss the range of applicability of our results.

Modelling accuracy—A limitation of our method is the accuracy of our results, which we demonstrate hold to $\mathcal{O}(1)$. However, we consider this sufficient to identify different scenario types, given the current level of uncertainties on both the observations and the modelling. We remind the reader of the uncertain hydrodynamic treatment of the blast wave and relativistic shock, neglecting any feedback from magnetic fields and non-thermal particles, as well as the uncertain treatment of the particle acceleration to a simple power-law injection spectrum.

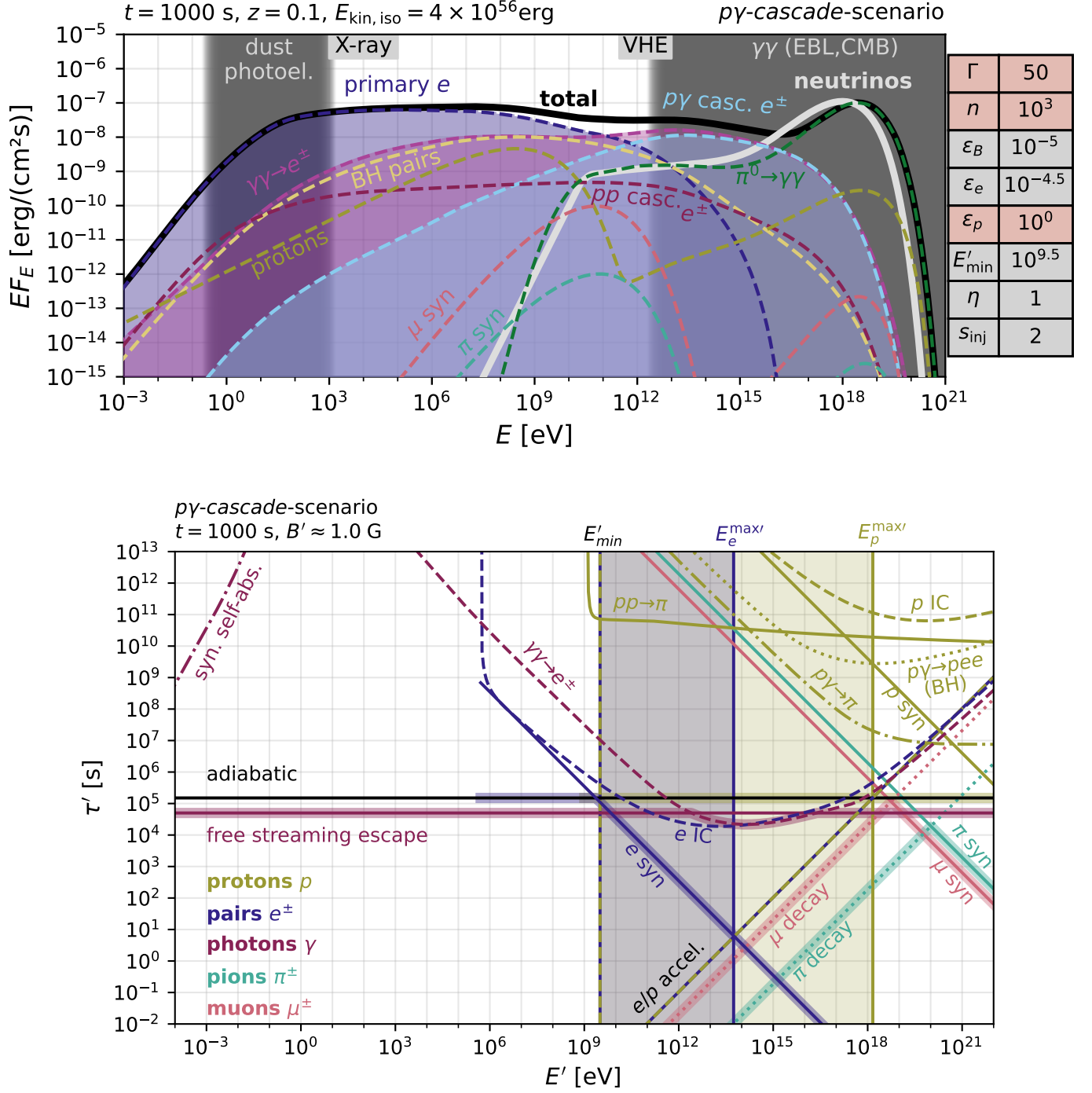


Figure 9. *py-cascade scenario (time-dependent method)* — **Top:** Observed energy flux as a function of observed energy for a representative parameter choice (for a detailed description of the figure see Figure 5 and 7, note n in cm⁻³ and E'_{min} in eV). We highlighted the density n , the shock Lorentz factor Γ , and the parameter ε_p due to their extreme combination of values. **Bottom:** Comoving time scales (for a detailed description of the figure see Figure 2 and 7).

Thermal particles—The description of the bulk thermal particle population and its transition to the non-thermal population at the injection (energy) scale are still subject to large uncertainty (Warren et al. 2018). In light of current particle-in-cell (PIC) simulations a prominent⁵ thermal peak would be expected in the proton and electron (and other secondary) spectral energy distributions (e.g. Marcowith et al. 2016). Besides the direct effect of signatures in the synchrotron spectrum at lower energies, this thermal particle population would also impact the SSC spectrum (Warren et al. 2022), as well as the proton target density of this paper’s *pp*-cascade scenario. An exploration of these signatures is beyond the scope of this paper.

Surrounding density profile—As a representative situation we focus our work on the case of a constant density profile for the surrounding gas. However, even for a steeper wind density profile, for which $n \propto r_\star^{-2}$, the recently swept-up volume scales as $\approx r_\star^3$, such that the spectra are still expected to be dominated by the most recently injected particles (as they are for the constant density case). It is therefore expected that the emission spectra are only affected at the $\mathcal{O}(1)$ level by such a modification to the injection history. We leave a more detailed investigation in this direction to future work.

Observed time—We focus on $t = 1000$ s as a representative time of *VHE* observations of GRB afterglows. However, the observed time only impacts the Lorentz factor $\Gamma \propto t^{-(3-w)/(8-2w)}$, and the density $n \propto r_\star^{-w} \propto t^{-w/(4-w)}$ (Zhang 2018). For values of $0 \leq w \leq 2$ the scaling indices are at most 1 (or rather -1). This changes the location of our scenarios in the parameter space moderately, but we would expect no new types of solutions to arise from a change of this observation time focus.

Parameter scan and model selection—We performed a grid scan of the parameter space, exploring a finite volume with finite grid spacing. Given the large covered volume of the parameter space, it seems reasonable to consider it sufficiently exhaustive. The limited grid resolution and our simplified model selection process do not impact our qualitative conclusions focusing on possible scenarios.

5.2. Energetics

In terms of required energy, in particular the *p γ -cascade* scenario’s combination of $\Gamma = 50$ and $n =$

⁵ It should be noted that a hydrodynamic shock treatment is valid only for $\varepsilon_{\text{thermal}} \gg \varepsilon_e, \varepsilon_p$, in which case the thermal peak sticks out clearly over the non-thermal power-law.

10^3 cm^{-3} requires at $t = 10^3$ s a seemingly large $E_{\text{kin,iso}} \approx 4 \times 10^{56}$ erg compared to observed photon fluences. However, from a theoretical perspective, we place this in the context of the energy released by the core collapse of a massive rotating star, by making the following simplifying assumptions: From the accreted mass $M \approx 10M_\odot$ a fraction $\varepsilon_{\text{kin}} \approx 0.1$ can be converted to kinetic energy, which is directed into a cone with opening angle $\theta \approx 3^\circ$, giving:

$$E_{\text{kin,iso}} \approx 10^{57} \text{ erg} \left(\frac{M}{10M_\odot} \right) \left(\frac{\varepsilon_{\text{kin}}}{0.1} \right) \left(\frac{3^\circ}{\theta} \right)^2 \quad (18)$$

This estimate aligns with findings of values up to $E_{\text{kin,iso}} \approx 10^{56}$ erg in prompt emission internal shock models if GRBs are to power the UHECRs (Heinze et al. 2020), for which even larger values of $E_{\text{kin,iso}}$ are still consistent given the uncertainties in the energy dissipation efficiencies in the prompt phase. Furthermore, if the engine is a newly formed accreting black hole or magnetar, the rotational energy that can be extracted from the system can be estimated as $E_{\text{kin,iso}} \simeq 10^{56}$ erg for a solar-mass black hole and a jet opening angle of 3.5° , see discussion in Rudolph et al. (2023). We conclude that the energetic requirements to make hadronic components relevant to the SED are optimistic but not impossible.

5.3. Ultra-High-Energy Cosmic Rays

In particular the *Proton-syn* and the *p γ -cascade* scenarios lead to the creation of UHECRs above observed energies of $E_p \approx 10^{18}$ eV. One can assume that a fraction of the highest-energy particles is no longer efficiently linked to the plasma, and instead of adiabatically cooling escapes from the blast wave at a similar time scale t'_{esc} . One may especially expect that UHECRs can efficiently escape as soon as the Larmor radius becomes comparable to the size of the region; see, e.g., discussion in Baerwald et al. (2013). We note that this transition could lead to a spectral signature for the protons at the highest energies, and therefore also for the proton-synchrotron photons and secondary cascade particles.

We can parameterise this escape with an uncertain efficiency factor $\varepsilon_{\text{esc}} \lesssim 1$ and a bolometric factor $f_{\text{bol}} \lesssim 1$ that depends on the energy range where escape dominates. In the upstream or progenitor rest frame, we estimate the total injected energy into the UHECR population simply as

$$E_{\text{UHECR,iso}} \approx \varepsilon_{\text{esc}} f_{\text{bol}} \varepsilon_p E_{\text{kin,iso}}. \quad (19)$$

We highlight, that the isotropic equivalent energy is considered here, since GRB jets not pointing at us also contribute to the UHECR flux at Earth.

The required energy output in UHECRs per GRB is about $E_{\text{UHECR,iso}} \simeq 10^{53}$ erg if GRBs are to be the sources of the UHECRs (see Baerwald et al. (2015) for a more detailed discussion). Therefore, if all GRBs were alike our prototype, and happened at a rate of $1 \text{ Gpc}^{-3} \text{ yr}^{-1}$, GRBs could comfortably power the UHECRs in the *Proton-syn* and *p γ -cascade* scenarios.

However, the assumption $\varepsilon_p \simeq 1$, suggesting that most of the kinetic energy would be dissipated into UHECRs, requires further investigation as of feedback on the background thermal shock assumed. Furthermore, we note that current observations favour a UHECR composition including also masses larger than just pure proton as simplified in this work (e.g. Heinze et al. 2019).

5.4. Model Distinction

The presented scenarios are by construction hard to distinguish in the keV–TeV energy range. Full observational coverage of the keV–TeV range remains still crucial, and contemporaneous data is needed to confirm the emerging single power-law nature of the spectrum at a statistically significant level.

The scenarios which we find could be distinguished via an accurate measurement of the photon index at the highest observable energies (≈ 10 TeV), where the *SSC* and *Proton-syn* scenarios are very soft ($\gamma \gg 2$), whereas the other models continue hard ($\gamma \approx 2$). However, the the EBL absorption would allow the observation of a GRB at such high energies only for a very close event ($z \lesssim 0.01$).

In principle, an additional distinction could be based on the neutrino flux (high in *p γ -cascade* scenario), although this seems challenging with even future instruments (compare Figure 12).

Besides their spectra and possible neutrino signatures, the other observational dimension of GRB afterglows is their evolution with time. In principle the temporal evolution of the relative ratio between low (electron synchrotron) and high energy component (differs per scenario) is another way of distinguishing between these scenarios. However, the deceleration of the emitting blast wave mixes the temporal evolution of the flux at a fixed emitted energy with an additional drift of the spectrum towards lower energies. A robust determination of the scaling of both effects is challenging due to the uncertainties in the density profile around the GRB and observationally the fast decaying light curves (temporal power-law index $\alpha \lesssim -1$, with $EF_E \propto t^\alpha$).

6. CONCLUSIONS

The emerging observational picture of VHE detected GRBs (especially GRB 190114C, GRB 190829A and GRB 221009A) indicates a flat (i.e. $\gamma \approx 2 - 2.2$), single power-law spectrum from keV to TeV energies, extending even beyond 10 TeV for GRB 221009A. In this paper, we perform a systematic exploration of the possibilities of a one-zone, lepto-hadronic, relativistic-shock model to reproduce this behaviour.

We find five possible scenarios (see Table 3): *SSC*, *Extended-syn*, *Proton-syn*, *pp-cascade* and *p γ -cascade*. No scenario matches all of the observational criteria in a convincing and exclusive manner. While for all of the scenarios the energy flux levels at keV and TeV energies are comparable, the modelled photon index at TeV energies does not reproduce the observed hard values ($\gamma \approx 2 - 2.2$) in the *SSC* and *Proton-syn* scenarios, which exhibit significant curvature. We find that this is different for the *pp-cascade* and *p γ -cascade* scenarios. These are embedded in higher density environments ($n \approx 10^2 - 10^4 \text{ cm}^{-3}$), such as typical for molecular clouds. Finally, the *Extended-syn* scenario also reproduces flat spectra to the highest energies in a plausible and simple manner, although the small value of η needed needs justifying (e.g. in an effective two-zone model).

From the observational perspective we find the need for improved coordinated multi-wavelength observations of the afterglow phase. Specifically, contemporaneous spectral coverage, logarithmically sampled in time and energy, is required to unveil the nature of the VHE emission. Future observational focus should be given: 1) to the keV–TeV range to test the flatness hypothesis; 2) to the highest energies (tens of TeV) to test the origin of the VHE emission. We find the power of neutrino constraints to be limited.

The authors would like to thank Pavlo Plotko for helpful input on the grid scan using the `PrINCE analysis tool` and Sylvia Zhu for helpful feedback on the paper. This work was supported by the International Helmholtz-Weizmann Research School for Multimessenger Astronomy, largely funded through the Initiative and Networking Fund of the Helmholtz Association. All figures by the authors under a [CC BY 4.0 license](#).

Software: NumPy (Harris et al. 2020), Matplotlib (Hunter 2007), Astropy (Astropy Collaboration et al. 2022), pybind11 (Jakob et al. 2017), Eigen (Guennebaud et al. 2010), AM³ (Klinger et al. 2023b), PrINCE analysis tool (Heinze 2020), color schemes (Tol 2021)

APPENDIX

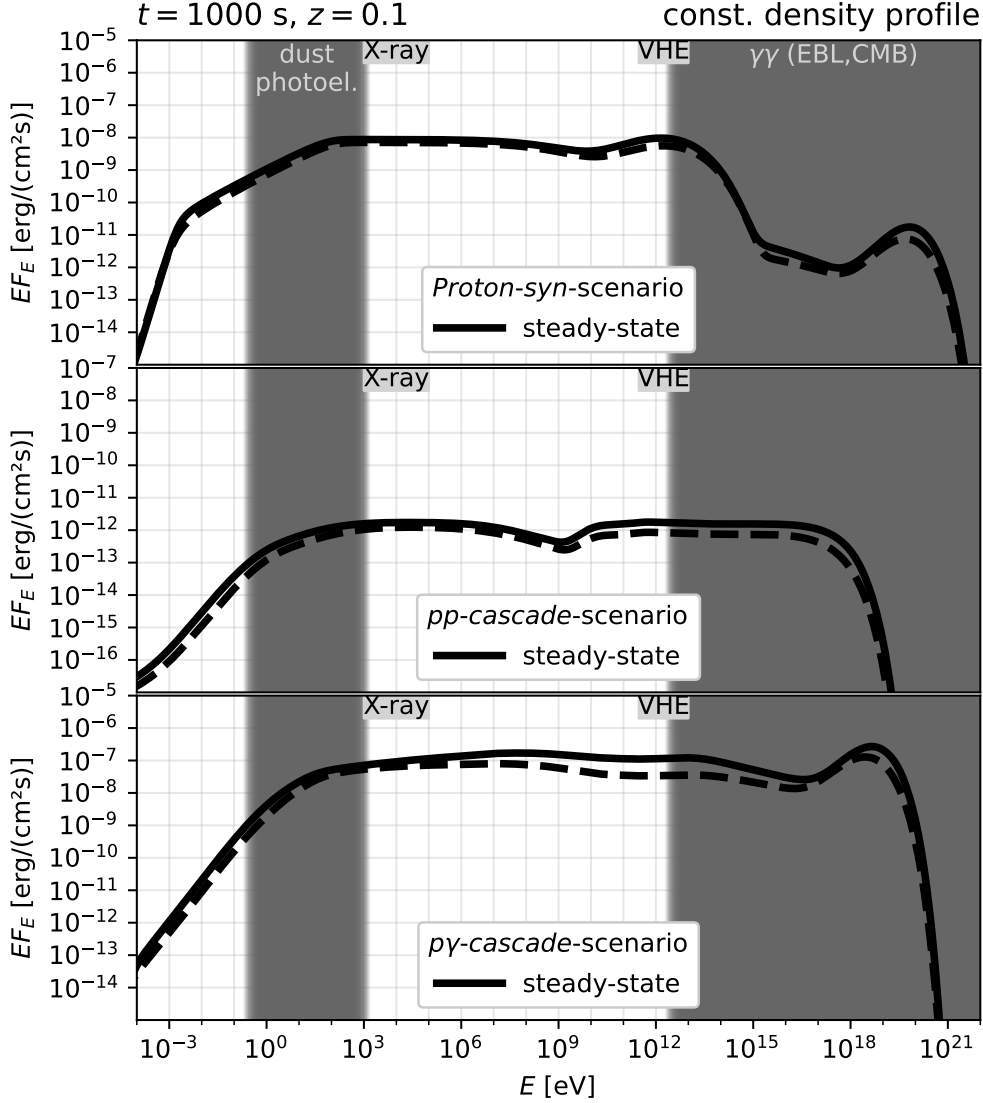


Figure 10. Comparison of the SEDs for the hadronic scenarios in the *steady-state* and *time-dependent* method, analogous to Figure 3.

A. QUASI-STEADY-STATE APPROXIMATION FOR HADRONIC SCENARIOS

We present in Figure 10 a comparison of the *time-dependent* and *steady-state* methods applied to our three hadronic cases. Both methods agree also for these cases well up to $\mathcal{O}(1)$. We note that for the *Extended-syn* scenario the curves agree similarly well as the synchrotron components in all scenarios; see, e.g., Figure 3.

B. EXEMPLARY PARTICLE DISTRIBUTION FOR *Proton-syn* SCENARIO

As an example, and for intuition, we give in Figure 11 the comoving energy spectra of the radiating particles at $t = 1000$ s, belonging to the *Proton-syn* scenario in Section 4.3.

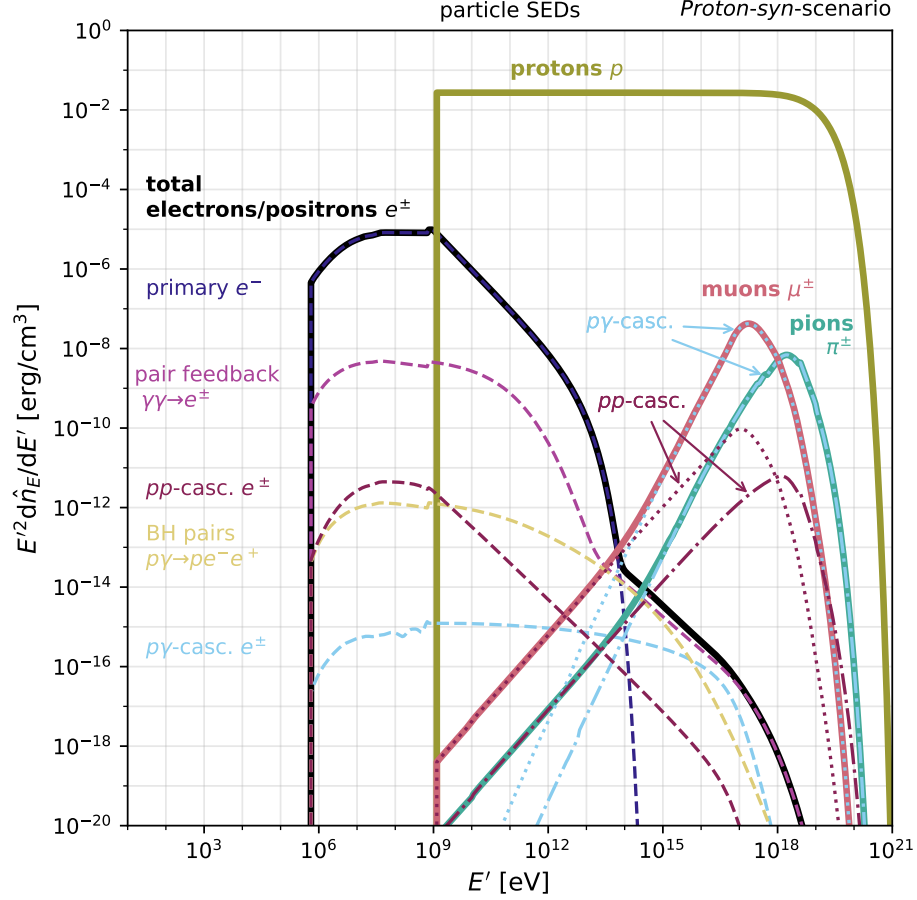


Figure 11. Comoving particle distributions for protons, electrons (including positrons), pions and muons for the *Proton-syn* scenario at observed time $t = 1000$ s.

C. NEUTRINO FLUENCES

It is useful to discuss the detectability of these scenarios with current and future neutrino telescopes. We show in Figure 12 a simple approximation for the neutrino fluence, $t \times E_\nu F_{E_\nu}$. The comparison to existing and future detectors shows that the neutrinos for the *Proton-syn* and *pp-cascade* scenarios are far below the sensitivity, whereas the extreme *p\gamma-cascade* scenario touches the IceCube-Gen2 sensitivity curve, which implies that the neutrino fluences from GRBs with parameters resembling our *p\gamma-cascade* scenario could reach the detectable level for IceCube-Gen2. However, this conclusion depends on many factors, such as the duration and the distance to the observers.

REFERENCES

- Abbasi, R., et al. 2021, PoS, ICRC2021, 1183, doi: [10.22323/1.395.1183](https://doi.org/10.22323/1.395.1183)
- Ackermann, M., Ajello, M., Asano, K., et al. 2014, Science, 343, 42, doi: [10.1126/science.1242353](https://doi.org/10.1126/science.1242353)
- Ajello, M., Baldini, L., Barbiellini, G., et al. 2018, ApJ, 863, 138, doi: [10.3847/1538-4357/aad000](https://doi.org/10.3847/1538-4357/aad000)
- Ajello, M., Arimoto, M., Axelsson, M., et al. 2019, ApJ, 878, 52, doi: [10.3847/1538-4357/ab1d4e](https://doi.org/10.3847/1538-4357/ab1d4e)
- . 2020, ApJ, 890, 9, doi: [10.3847/1538-4357/ab5b05](https://doi.org/10.3847/1538-4357/ab5b05)
- Álvarez-Muñiz, J., Alves Batista, R., Balagopal V., A., et al. 2020, Science China Physics, Mechanics, and Astronomy, 63, 219501, doi: [10.1007/s11433-018-9385-7](https://doi.org/10.1007/s11433-018-9385-7)
- Asano, K., Murase, K., & Toma, K. 2020, ApJ, 905, 105, doi: [10.3847/1538-4357/abc82c](https://doi.org/10.3847/1538-4357/abc82c)
- Astropy Collaboration, Price-Whelan, A. M., Lim, P. L., et al. 2022, ApJ, 935, 167, doi: [10.3847/1538-4357/ac7c74](https://doi.org/10.3847/1538-4357/ac7c74)
- Baerwald, P., Bustamante, M., & Winter, W. 2013, ApJ, 768, 186, doi: [10.1088/0004-637X/768/2/186](https://doi.org/10.1088/0004-637X/768/2/186)

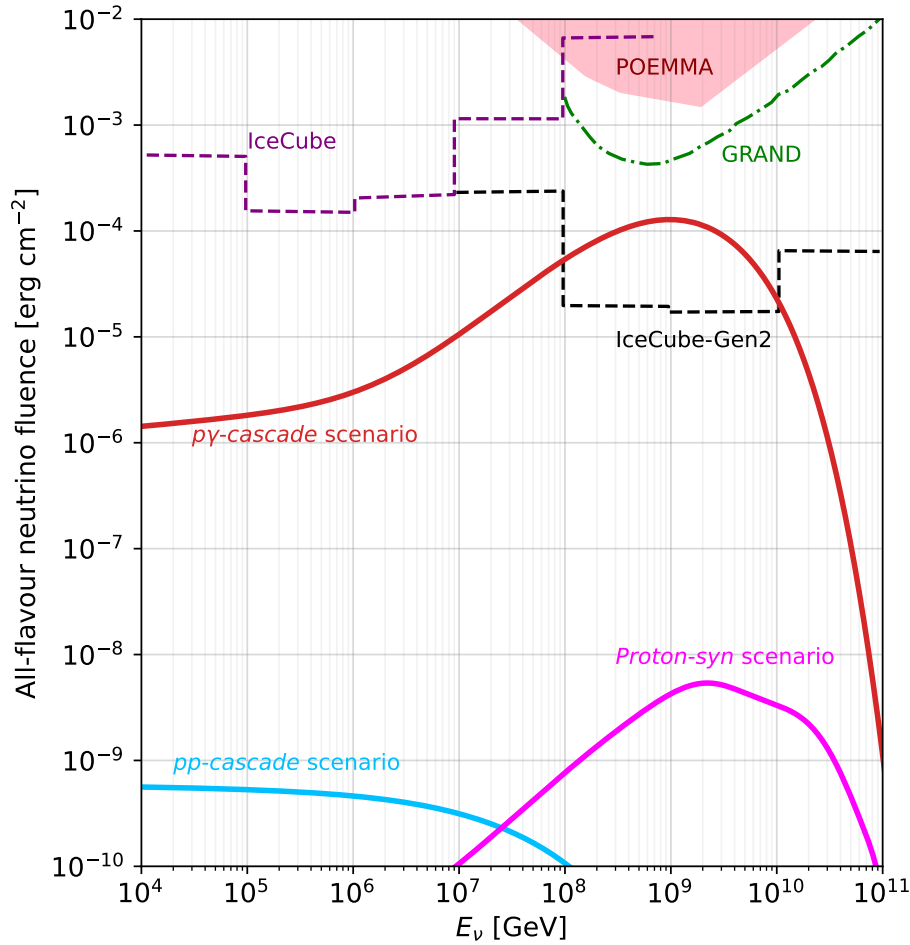


Figure 12. All-flavor neutrino fluences of the *Proton-syn*, *pp-cascade* and *p γ -cascade* scenarios approximated by the product of the neutrino energy flux $E_\nu F_{E_\nu}$ multiplied with the observed time $t = 10^3$ s. For comparison we show the sensitivity curves of current and future neutrino detectors, such as IceCube, IceCube-Gen2 (Abbasi et al. 2021), GRAND (Álvarez-Muñiz et al. 2020), and POEMMA (Venters et al. 2020).

- . 2015, *Astroparticle Physics*, 62, 66,
doi: [10.1016/j.astropartphys.2014.07.007](https://doi.org/10.1016/j.astropartphys.2014.07.007)
- Bell, A. R., Araudo, A. T., Matthews, J. H., & Blundell, K. M. 2018, *MNRAS*, 473, 2364,
doi: [10.1093/mnras/stx2485](https://doi.org/10.1093/mnras/stx2485)
- Beloborodov, A. M. 2002, *ApJ*, 565, 808,
doi: [10.1086/324195](https://doi.org/10.1086/324195)
- Beloborodov, A. M., & Mészáros, P. 2017, *SSRv*, 207, 87,
doi: [10.1007/s11214-017-0348-6](https://doi.org/10.1007/s11214-017-0348-6)
- Berezinsky, V., & Kalashev, O. 2016, *PhRvD*, 94, 023007,
doi: [10.1103/PhysRevD.94.023007](https://doi.org/10.1103/PhysRevD.94.023007)
- Blandford, R. D., & McKee, C. F. 1976, *Physics of Fluids*, 19, 1130, doi: [10.1063/1.861619](https://doi.org/10.1063/1.861619)
- Bohm, D. 1949, *Qualitative Description of the Arc Plasma in a Magnetic Field*.
<https://cir.nii.ac.jp/crid/1570009750450419968>
- Cao, Z., Aharonian, F., An, Q., et al. 2023, *Science Advances*, 9, eadj2778, doi: [10.1126/sciadv.adj2778](https://doi.org/10.1126/sciadv.adj2778)
- Chiang, J., & Dermer, C. D. 1999, *ApJ*, 512, 699,
doi: [10.1086/306789](https://doi.org/10.1086/306789)
- Das, S., & Razzaque, S. 2023, *A&A*, 670, L12,
doi: [10.1051/0004-6361/202245377](https://doi.org/10.1051/0004-6361/202245377)

- Derishev, E., & Piran, T. 2021, *ApJ*, 923, 135, doi: [10.3847/1538-4357/ac2dec](https://doi.org/10.3847/1538-4357/ac2dec)
- Derishev, E. V., & Piran, T. 2016, *MNRAS*, 460, 2036, doi: [10.1093/mnras/stw1175](https://doi.org/10.1093/mnras/stw1175)
- Fan, Y.-Z., Piran, T., Narayan, R., & Wei, D.-M. 2008, *MNRAS*, 384, 1483, doi: [10.1111/j.1365-2966.2007.12765.x](https://doi.org/10.1111/j.1365-2966.2007.12765.x)
- Fukushima, T., To, S., Asano, K., & Fujita, Y. 2017, *ApJ*, 844, 92, doi: [10.3847/1538-4357/aa7b83](https://doi.org/10.3847/1538-4357/aa7b83)
- Gao, S., Fedynitch, A., Winter, W., & Pohl, M. 2019, *Nature Astron.*, 3, 88, doi: [10.1038/s41550-018-0610-1](https://doi.org/10.1038/s41550-018-0610-1)
- Gao, S., Fedynitch, A., Winter, W., & Pohl, M. 2019, *Nature Astronomy*, 3, 88, doi: [10.1038/s41550-018-0610-1](https://doi.org/10.1038/s41550-018-0610-1)
- Ghisellini, G., Ghirlanda, G., Oganessian, G., et al. 2020, *A&A*, 636, A82, doi: [10.1051/0004-6361/201937244](https://doi.org/10.1051/0004-6361/201937244)
- Giannios, D., & Spruit, H. C. 2005, *A&A*, 430, 1, doi: [10.1051/0004-6361:20047033](https://doi.org/10.1051/0004-6361:20047033)
- Gill, R., & Granot, J. 2023, *MNRAS*, 524, L78, doi: [10.1093/mnras/slad075](https://doi.org/10.1093/mnras/slad075)
- Grošelj, D., Sironi, L., & Beloborodov, A. M. 2022, *ApJ*, 933, 74, doi: [10.3847/1538-4357/ac713e](https://doi.org/10.3847/1538-4357/ac713e)
- Guarini, E., Tamborra, I., Bégué, D., & Rudolph, A. 2023, *MNRAS*, 523, 149, doi: [10.1093/mnras/stad1421](https://doi.org/10.1093/mnras/stad1421)
- Guennebaud, G., Jacob, B., et al. 2010, *Eigen v3*, <http://eigen.tuxfamily.org>
- H. E. S. S. Collaboration, Abdalla, H., Abramowski, A., et al. 2017, *A&A*, 606, A59, doi: [10.1051/0004-6361/201731200](https://doi.org/10.1051/0004-6361/201731200)
- H. E. S. S. Collaboration, Abdalla, H., Aharonian, F., et al. 2021, *Science*, 372, 1081, doi: [10.1126/science.abe8560](https://doi.org/10.1126/science.abe8560)
- Harris, C. R., Millman, K. J., van der Walt, S. J., et al. 2020, *Nature*, 585, 357, doi: [10.1038/s41586-020-2649-2](https://doi.org/10.1038/s41586-020-2649-2)
- Heinze, J. 2020, *PriNCE analysis tool*
- Heinze, J., Biehl, D., Fedynitch, A., et al. 2020, *MNRAS*, 498, 5990, doi: [10.1093/mnras/staa2751](https://doi.org/10.1093/mnras/staa2751)
- Heinze, J., Fedynitch, A., Boncioli, D., & Winter, W. 2019, *ApJ*, 873, 88, doi: [10.3847/1538-4357/ab05ce](https://doi.org/10.3847/1538-4357/ab05ce)
- H.E.S.S. Collaboration, Abdalla, H., Adam, R., et al. 2019, *Nature*, 575, 464, doi: [10.1038/s41586-019-1743-9](https://doi.org/10.1038/s41586-019-1743-9)
- Huang, Z.-Q., Kirk, J. G., Giacinti, G., & Reville, B. 2022, *ApJ*, 925, 182, doi: [10.3847/1538-4357/ac3f38](https://doi.org/10.3847/1538-4357/ac3f38)
- Hunter, J. D. 2007, *Computing in Science & Engineering*, 9, 90, doi: [10.1109/MCSE.2007.55](https://doi.org/10.1109/MCSE.2007.55)
- Isravel, H., Bégué, D., & Pe'er, A. 2023a, *ApJ*, 956, 12, doi: [10.3847/1538-4357/acefcd](https://doi.org/10.3847/1538-4357/acefcd)
- Isravel, H., Pe'er, A., & Bégué, D. 2023b, *ApJ*, 955, 70, doi: [10.3847/1538-4357/acec73](https://doi.org/10.3847/1538-4357/acec73)
- Jakob, W., Rhineland, J., & Moldovan, D. 2017, *pybind11* – Seamless operability between C++11 and Python
- Khangulyan, D., Aharonian, F., Romoli, C., & Taylor, A. 2021, *ApJ*, 914, 76, doi: [10.3847/1538-4357/abfcbf](https://doi.org/10.3847/1538-4357/abfcbf)
- Khangulyan, D., Taylor, A. M., & Aharonian, F. 2023, *ApJ*, 947, 87, doi: [10.3847/1538-4357/acc24e](https://doi.org/10.3847/1538-4357/acc24e)
- Klinger, M., Tak, D., Taylor, A. M., & Zhu, S. J. 2023a, *MNRAS*, 520, 839, doi: [10.1093/mnras/stad142](https://doi.org/10.1093/mnras/stad142)
- Klinger, M., Taylor, A. M., Parsotan, T., et al. 2024, *MNRAS*, 529, L47, doi: [10.1093/mnras/lsad185](https://doi.org/10.1093/mnras/lsad185)
- Klinger, M., Rudolph, A., Rodrigues, X., et al. 2023b, *arXiv e-prints*, arXiv:2312.13371, doi: [10.48550/arXiv.2312.13371](https://doi.org/10.48550/arXiv.2312.13371)
- Kobayashi, S., Piran, T., & Sari, R. 1997, *ApJ*, 490, 92, doi: [10.1086/512791](https://doi.org/10.1086/512791)
- Kouveliotou, C., Granot, J., Racusin, J. L., et al. 2013, *ApJL*, 779, L1, doi: [10.1088/2041-8205/779/1/L1](https://doi.org/10.1088/2041-8205/779/1/L1)
- Lesage, S., Veres, P., Briggs, M. S., et al. 2023, *ApJL*, 952, L42, doi: [10.3847/2041-8213/ace5b4](https://doi.org/10.3847/2041-8213/ace5b4)
- LHAASO Collaboration, Cao, Z., Aharonian, F., et al. 2023, *Science*, 380, 1390, doi: [10.1126/science.adg9328](https://doi.org/10.1126/science.adg9328)
- Liu, R.-Y., Zhang, H.-M., & Wang, X.-Y. 2023, *ApJL*, 943, L2, doi: [10.3847/2041-8213/acaf5e](https://doi.org/10.3847/2041-8213/acaf5e)
- MAGIC Collaboration, Acciari, V. A., Ansoldi, S., et al. 2019a, *Nature*, 575, 455, doi: [10.1038/s41586-019-1750-x](https://doi.org/10.1038/s41586-019-1750-x)
- . 2019b, *Nature*, 575, 459, doi: [10.1038/s41586-019-1754-6](https://doi.org/10.1038/s41586-019-1754-6)
- Marcowith, A., Bret, A., Bykov, A., et al. 2016, *Reports on Progress in Physics*, 79, 046901, doi: [10.1088/0034-4885/79/4/046901](https://doi.org/10.1088/0034-4885/79/4/046901)
- Mészáros, P. 2006, *Reports on Progress in Physics*, 69, 2259, doi: [10.1088/0034-4885/69/8/R01](https://doi.org/10.1088/0034-4885/69/8/R01)
- Meszáros, P., Rees, M. J., & Papathanassiou, H. 1994, *ApJ*, 432, 181, doi: [10.1086/174559](https://doi.org/10.1086/174559)
- Misra, K., Resmi, L., Kann, D. A., et al. 2021, *MNRAS*, 504, 5685, doi: [10.1093/mnras/stab1050](https://doi.org/10.1093/mnras/stab1050)
- Mochkovitch, R., & Daigne, F. 1998, in *American Institute of Physics Conference Series*, Vol. 428, *Gamma-Ray Bursts*, 4th Hunstville Symposium, ed. C. A. Meegan, R. D. Preece, & T. M. Koshut, 667–671, doi: [10.1063/1.55396](https://doi.org/10.1063/1.55396)
- Murase, K., Toomey, M. W., Fang, K., et al. 2018, *ApJ*, 854, 60, doi: [10.3847/1538-4357/aaa48a](https://doi.org/10.3847/1538-4357/aaa48a)
- O'Connor, B., Troja, E., Ryan, G., et al. 2023, *Science Advances*, 9, eadi1405, doi: [10.1126/sciadv.adi1405](https://doi.org/10.1126/sciadv.adi1405)
- Pe'er, A., & Ryde, F. 2018, in *Fourteenth Marcel Grossmann Meeting - MG14*, ed. M. Bianchi, R. T. Jansen, & R. Ruffini, 806–840, doi: [10.1142/9789813226609_0044](https://doi.org/10.1142/9789813226609_0044)
- Pe'er, A., & Waxman, E. 2005, *ApJ*, 628, 857, doi: [10.1086/431139](https://doi.org/10.1086/431139)
- Pei, Y. C. 1992, *ApJ*, 395, 130, doi: [10.1086/171637](https://doi.org/10.1086/171637)

- Pennanen, T., Vurm, I., & Poutanen, J. 2014, *A&A*, 564, A77, doi: [10.1051/0004-6361/201322520](https://doi.org/10.1051/0004-6361/201322520)
- Petropoulou, M., & Mastichiadis, A. 2009, *A&A*, 507, 599, doi: [10.1051/0004-6361/200912970](https://doi.org/10.1051/0004-6361/200912970)
- Piran, T. 2004, *Reviews of Modern Physics*, 76, 1143, doi: [10.1103/RevModPhys.76.1143](https://doi.org/10.1103/RevModPhys.76.1143)
- Planck Collaboration, Aghanim, N., Akrami, Y., et al. 2020, *A&A*, 641, A6, doi: [10.1051/0004-6361/201833910](https://doi.org/10.1051/0004-6361/201833910)
- Ressler, S. M., & Laskar, T. 2017, *ApJ*, 845, 150, doi: [10.3847/1538-4357/aa8268](https://doi.org/10.3847/1538-4357/aa8268)
- Rodrigues, X., Garrappa, S., Gao, S., et al. 2021, *ApJ*, 912, 54, doi: [10.3847/1538-4357/abe87b](https://doi.org/10.3847/1538-4357/abe87b)
- Rudolph, A., Petropoulou, M., Winter, W., & Bošnjak, Ž. 2023, *ApJL*, 944, L34, doi: [10.3847/2041-8213/acb6d7](https://doi.org/10.3847/2041-8213/acb6d7)
- Ryan, G., van Eerten, H., Piro, L., & Troja, E. 2020, *ApJ*, 896, 166, doi: [10.3847/1538-4357/ab93cf](https://doi.org/10.3847/1538-4357/ab93cf)
- Sari, R., & Esin, A. A. 2001, *ApJ*, 548, 787, doi: [10.1086/319003](https://doi.org/10.1086/319003)
- Sari, R., Narayan, R., & Piran, T. 1996, *ApJ*, 473, 204, doi: [10.1086/178136](https://doi.org/10.1086/178136)
- Sato, Y., Murase, K., Ohira, Y., & Yamazaki, R. 2023, *MNRAS*, 522, L56, doi: [10.1093/mnrasl/slad038](https://doi.org/10.1093/mnrasl/slad038)
- Senno, N., Mészáros, P., Murase, K., Baerwald, P., & Rees, M. J. 2015, *ApJ*, 806, 24, doi: [10.1088/0004-637X/806/1/24](https://doi.org/10.1088/0004-637X/806/1/24)
- Tavani, M., Piano, G., Bulgarelli, A., et al. 2023, *ApJL*, 956, L23, doi: [10.3847/2041-8213/accaff](https://doi.org/10.3847/2041-8213/accaff)
- Tol, P. 2021, INTRODUCTION TO COLOUR SCHEMES, <https://personal.sron.nl/~pault/>, Accessed: 2024-03-12
- van der Horst, A. J., Paragi, Z., de Bruyn, A. G., et al. 2014, *MNRAS*, 444, 3151, doi: [10.1093/mnras/stu1664](https://doi.org/10.1093/mnras/stu1664)
- van Eerten, H., Zhang, W., & MacFadyen, A. 2010, *ApJ*, 722, 235, doi: [10.1088/0004-637X/722/1/235](https://doi.org/10.1088/0004-637X/722/1/235)
- Vanthieghem, A., Lemoine, M., Plotnikov, I., et al. 2020, *Galaxies*, 8, 33, doi: [10.3390/galaxies8020033](https://doi.org/10.3390/galaxies8020033)
- Venters, T. M., Reno, M. H., Krizmanic, J. F., et al. 2020, *PhRvD*, 102, 123013, doi: [10.1103/PhysRevD.102.123013](https://doi.org/10.1103/PhysRevD.102.123013)
- Vietri, M. 1995, *ApJ*, 453, 883, doi: [10.1086/176448](https://doi.org/10.1086/176448)
- Wang, K., Tang, Q.-W., Zhang, Y.-Q., et al. 2023, *arXiv e-prints*, arXiv:2310.11821, doi: [10.48550/arXiv.2310.11821](https://doi.org/10.48550/arXiv.2310.11821)
- Warren, D. C., Barkov, M. V., Ito, H., Nagataki, S., & Laskar, T. 2018, *MNRAS*, 480, 4060, doi: [10.1093/mnras/sty2138](https://doi.org/10.1093/mnras/sty2138)
- Warren, D. C., Dainotti, M., Barkov, M. V., et al. 2022, *ApJ*, 924, 40, doi: [10.3847/1538-4357/ac2f43](https://doi.org/10.3847/1538-4357/ac2f43)
- Warren, D. C., Ellison, D. C., Bykov, A. M., & Lee, S.-H. 2015, *MNRAS*, 452, 431, doi: [10.1093/mnras/stv1304](https://doi.org/10.1093/mnras/stv1304)
- Waxman, E. 1995, *PhRvL*, 75, 386, doi: [10.1103/PhysRevLett.75.386](https://doi.org/10.1103/PhysRevLett.75.386)
- Willingale, R., Starling, R. L. C., Beardmore, A. P., Tanvir, N. R., & O'Brien, P. T. 2013, *MNRAS*, 431, 394, doi: [10.1093/mnras/stt175](https://doi.org/10.1093/mnras/stt175)
- Wilms, J., Allen, A., & McCray, R. 2000, *ApJ*, 542, 914, doi: [10.1086/317016](https://doi.org/10.1086/317016)
- Yuan, C., Mészáros, P., Murase, K., & Jeong, D. 2018, *ApJ*, 857, 50, doi: [10.3847/1538-4357/aab774](https://doi.org/10.3847/1538-4357/aab774)
- Yuan, C., Murase, K., Guetta, D., et al. 2022, *ApJ*, 932, 80, doi: [10.3847/1538-4357/ac6ddf](https://doi.org/10.3847/1538-4357/ac6ddf)
- Zhang, B. 2018, *The Physics of Gamma-Ray Bursts*, doi: [10.1017/9781139226530](https://doi.org/10.1017/9781139226530)
- Zhang, B., & Yan, H. 2011, *ApJ*, 726, 90, doi: [10.1088/0004-637X/726/2/90](https://doi.org/10.1088/0004-637X/726/2/90)
- Zhang, B. T., Murase, K., Ioka, K., et al. 2023a, *ApJL*, 947, L14, doi: [10.3847/2041-8213/acc79f](https://doi.org/10.3847/2041-8213/acc79f)
- Zhang, B. T., Murase, K., Yuan, C., Kimura, S. S., & Mészáros, P. 2021, *ApJL*, 908, L36, doi: [10.3847/2041-8213/abe0b0](https://doi.org/10.3847/2041-8213/abe0b0)
- Zhang, H., Christie, I. M., Petropoulou, M., Rueda-Becerril, J. M., & Giannios, D. 2020, *MNRAS*, 496, 974, doi: [10.1093/mnras/staa1583](https://doi.org/10.1093/mnras/staa1583)
- Zhang, H.-M., Huang, Y.-Y., Liu, R.-Y., & Wang, X.-Y. 2023b, *ApJL*, 956, L21, doi: [10.3847/2041-8213/acfcab](https://doi.org/10.3847/2041-8213/acfcab)